



Simple methods for satellite identification of algal blooms and species using 10-year time series data from the East China Sea



Fang Shen^{a,b,*}, Rugang Tang^a, Xuerong Sun^a, Dongyan Liu^a

^a State Key Laboratory of Estuarine and Coastal Research, East China Normal University, 500 Dongchuan Road, Shanghai, 200241, China

^b Institute of Eco-Chongming (IEC), 3663 Zhongshan N. Road, Shanghai, 200062, China

ARTICLE INFO

Keywords:

Algal blooms
Phytoplankton species
Diatom
Dinoflagellate
MERIS
MODIS
GOCI

ABSTRACT

Long-term ocean color satellite missions have the ability to help monitor algal blooms. However, satellite identification of algal blooms and species in turbid coastal waters has been challenging. There is an urgent need for simple and effective methods to identify locations, areas, durations, and species present in algal blooms through satellite observation, to aid in the operational and emergency monitoring of the marine environment. In this study, based on a three-band blended model, we propose an indicator (Red tide Detection Index, RDI) that is suitable for the purpose of detecting algal blooms in turbid coastal waters using multi-source ocean color data. MERIS, MODIS, and GOCI data used for the detection of algal blooms demonstrate consistent results using the RDI indicator, and these results correlate with *in situ* investigations. Furthermore, based on a green-red spectral slope, we propose a method that uses MERIS data to identify dominant species of diatoms and dinoflagellates in algal blooms in the East China Sea (ECS). The 10-year time series MERIS data collected between 2003 and 2012 indicates that algal bloom occurrences are mainly distributed in the nearshore areas of the ECS, and possess a distinct climatological cycle. The 10-year time series MERIS data help discriminate diatom and dinoflagellate blooms in the ECS, and show the dissimilarity in the seasonal timing of their life cycles. We find that these two dominant species in algal blooms are usually distributed in different spatial locations in the ECS. Additionally, by defining a divergence index (DI), the limitations of spectral resolutions of satellite data used for algal bloom species differentiation are quantitatively assessed.

1. Introduction

Algal blooms can cause widespread ecological disasters across the world. The occurrence of algal blooms may lead to coastal hypoxia and toxin accumulation, water quality degradation, as well as, fishery and aquaculture activities collapses (Hallegraeff et al., 2003). The toxic species present in algal blooms pose a threat to human health via the aquatic food chain. The Marine Environment Quality Bulletin of the State Ocean Administration (SOA) reports that algal blooms occur almost every year between April and October in the East China Sea. In the bulletins of the SOA, algal blooms in the East China Sea are reported to be mainly dominated by the diatom species, *Skeletonema costatum*, and the dinoflagellate species, *Prorocentrum donghaiense*. Since 2005, toxic species, such as the dinoflagellate, *Karenia mikimotoi*, have also been occasionally observed.

Due to the complexity of the formation process and the triggering mechanisms of algal blooms, it is difficult to predict and prepare for their occurrence, in terms of time, location, evolution duration,

distribution, and dominant species present. Traditional methods have not been able to successfully monitor algal blooms, because algal blooms appear suddenly and algae can accumulate rapidly over a short period of time. The use of remote sensing stands out from other approaches since it can provide a synoptic view and continually monitor of algal blooms every day or every hour at a large spatial scale.

The detection of algal blooms through remote sensing has become an important topic since ocean color satellite missions were launched at the end of last century (IOCCG, 2014). There are several types of approaches to detect algal blooms using ocean color satellite imagery, such as chlorophyll *a* concentration (Chla) based approach (e.g., He et al., 2013), Chla anomalies based approach (e.g., Stumpf et al., 2003), reflectance-blended indices based approach (e.g., Gower et al., 2005), and absorption-trait based approach (e.g., Sathyendranath et al., 2004).

The Chla based approach for algal bloom detection is somewhat challenging. Although higher Chla indicates a potential augmentation in algal cells, Chla is not a counterpart for algal cell abundance due to the phytoplankton diversity, in terms of cell size and species. Moreover,

* Corresponding author. State Key Laboratory of Estuarine and Coastal Research, East China Normal University, 500 Dongchuan Road, Shanghai, 200241, China.
E-mail address: fshen@sklec.ecnu.edu.cn (F. Shen).

in coastal waters, satellite estimation of Chla in high accuracy still remains difficult (Hu, 2009). Satellite outputs regarding Chla may often be overestimated in turbid coastal waters, e.g., in coastal waters of the East China Sea (He et al., 2013; Shen et al., 2010a; Shi and Wang, 2012). Thus, there is a high risk of false identification when using Chla to identify algal blooms in the region (He et al., 2013).

The anomaly of Chla, e.g., which was observed when a single Chla value was compared to the 60-day running mean value, was successfully used for routine detections of *Karenia brevis* blooms in the Gulf of Mexico (Stumpf et al., 2003; Tomlinson et al., 2004). However, the anomaly cannot be easily detected if algal bloom species have low cellular chlorophyll *a* content (Siswanto et al., 2013), or when the time series satellite data for the monthly averages are less representative, due to the limited available imagery affected by the cloud coverage in the coastal area.

There are several kinds of reflectance-based indices for algal bloom detection. A red tide index (RI) was proposed by Ahn and Shanmugam (2006) for the detection of algal blooms in turbid coastal waters by combining the normalized water-leaving radiance of the SeaWiFS bands at 510, 555, and 443 nm. Its function was also dependent on a prerequisite of high accuracy in atmospheric correction (Siswanto et al., 2013), which still remains a challenging task in optically complex and turbid coastal waters. Moreover, utilizing the blue-green spectral range for the RI estimation may also be impacted by absorptions due to colored dissolved organic matter (CDOM) and suspended particulate matter (SPM). The phytoplankton fluorescence line height (FLH) index and the maximum chlorophyll index (MCI) have potential to detect algal blooms in coastal waters (Gower et al., 2005; Hu et al., 2005; Ryan et al., 2009). However, their applications in turbid coastal waters may be hindered due to the presence of high scattering suspended solids in the waters (Hu et al., 2005; Shen et al., 2010a).

Furthermore, efforts to enhance the ability of satellites that can discriminate species of algal blooms have been made in oceanography and ocean color remote sensing communities (IOCCG, 2014), although historic and current satellite ocean color sensors have limitations in terms of the spectral resolution and characteristic waveband positions used for differentiating various species of algal blooms (e.g., Blondeau-Patissier et al., 2014; Mouw et al., 2015; and references therein). For instance, a spectrally-resolved reflectance model that can be applied to the SeaWiFS data for the discrimination of diatom and non-diatom species was proposed by Sathyendranath et al. (2004). This model should be modified based on region due to the variability in the optical properties of the diverse range of diatom species (Jackson et al., 2011). Recently, a data-driven supervised classification approach for MODIS and MERIS differentiation of algal blooms consisting of *K. mikimotoi* and *Phaeocystis globosa* in European coastal waters was adopted by Kurekin et al. (2014). Using MODIS ocean bands, a *K. mikimotoi* bloom was detected in the western part of Seto-Inland Sea, Japan (Siswanto et al., 2013). However, due to the low scattering of *K. mikimotoi* in the water, it was not easy to differentiate, especially amidst the high scattering of suspended solids present. Using combined MODIS band data, including ocean color bands and non-ocean bands, the discrimination of the dinoflagellate, *P. donghaiense*, in diatom blooms was successfully conducted (Tao et al., 2015). This approach used a threshold of remote-sensing reflectance (R_{rs}) at 555 nm for the discrimination process, which requires highly accurate atmospherically corrected R_{rs} values. However, the atmospheric correction has been challenging over optically complex and turbid coastal waters. In addition, the R_{rs} at 531 nm was required for the calculation of the threshold for species discrimination; this is unavailable for most ocean color sensors, even VIIRS, a MODIS successor. The absence of this band might limit the application of the proposed algorithm to other ocean color sensors, e.g., MERIS, GOCI, etc.

As mentioned earlier, these approaches proposed for detecting algal blooms and discriminating species in algal blooms using satellite data requires a specific sensor. So far, there has been very little

documentation about a method that is capable of applying multi-sensor satellite data and carrying out the cross-verification of multiple satellite inversion results. The limitations are also attributed to the existing differences in the spectral resolution and characteristic waveband positions of ocean color sensors, depending on the specific targets of the initial design and the possible considerations of technical costs and tradeoffs.

In this case, developing a method for multi-source satellite data can increase the spatial and temporal coverage of ocean observations, and fill the temporal gap that may exist between on-orbit and off-orbit observations in satellite time series data. It can also provide a greater chance for the cross-verification and validation between ground truth data and satellite observations. More importantly, it can provide opportunities for the development of further studies on phytoplankton phenology and their response to climate change.

The purpose of this study is to: (1) develop an approach for detecting algal blooms in turbid coastal waters without the prerequisite of highly accurate atmospheric correction data and complicated processing procedures, aiming at multi-source satellite data applications (e.g., MERIS, MODIS, GOCI, or their successors); (2) explore a method for discriminating dominant species present in algal blooms (e.g., dominant diatom and dinoflagellate species) and (3) analyze and discuss the limitations of spectral resolutions and their impact on the discrimination of algal bloom species.

2. Data

2.1. In situ data

The Changjiang (Yangtze) Estuary, the Zhejiang coast, and the nearshore of the South Yellow Sea (Fig. 1) are areas with frequent outbreaks of algal blooms. They are mainly affected by the Changjiang riverine plumes and the sea front in the East China Sea (Wang et al., 2019), where the waters are turbid, eutrophic, and optically complex (Lei, 2011).

We carried out cruise campaigns in the Changjiang (Yangtze) Estuary and its adjacent coast (YEC) in August 2013, and in the East China Sea (ECS) in June and July 2014. Algal bloom occurrences at a total of 17 stations (13 stations in the YEC in August 2013, and 4 stations in the ECS in June 2014) were observed (Fig. 1).

During the cruise campaigns, *in situ* spectroradiometric measurements were made above the water to collect remote sensing reflectance (R_{rs}) data by using the Hyperspectral Surface Acquisition System (HyperSAS, Sea-Bird Scientific Inc.), which concurrently measured sea surface upwelling radiance (L_u), downwelling sky radiance (L_s), and downwelling solar irradiance (E_s) at wavelengths from 350 to 900 nm with a 1 nm interval. Therefore, *in situ* R_{rs} data was obtained using the following equation: $R_{rs} = (L_u - \rho L_s)/E_s$, where ρ is the sea surface reflectance factor. The details are described in Shen et al. (2014) and Sokoletsky and Shen (2014). Due to the impact of sunlight illumination conditions and the narrow strip distribution of the algal blooms, the number of *in situ* R_{rs} values collected was limited. Data for R_{rs} was available only at nine of the 17 algal bloom stations (seven stations in the YEC and two stations in the ECS).

In situ water samples with a volume of 500 ml were collected from the sea surface at each station and were stored in a polyethylene container with neutral formaldehyde solution and sealed away from light in preparation for identification. Algal species and cell counts of phytoplankton were identified using optical microscopy with a magnification of 200–400 times after the samples were set aside for 48 h, so that the supernatant fluid could be removed and each sample reconstituted to 100 ml. The species with a cell density larger than 1×10^4 cells per milliliter were considered as the dominant algal species in the bloom (Liu et al., 2015) and are shown in Table 1. The *in situ* data was also used for the validation of the satellite-based results obtained for algal bloom detection and species identification.

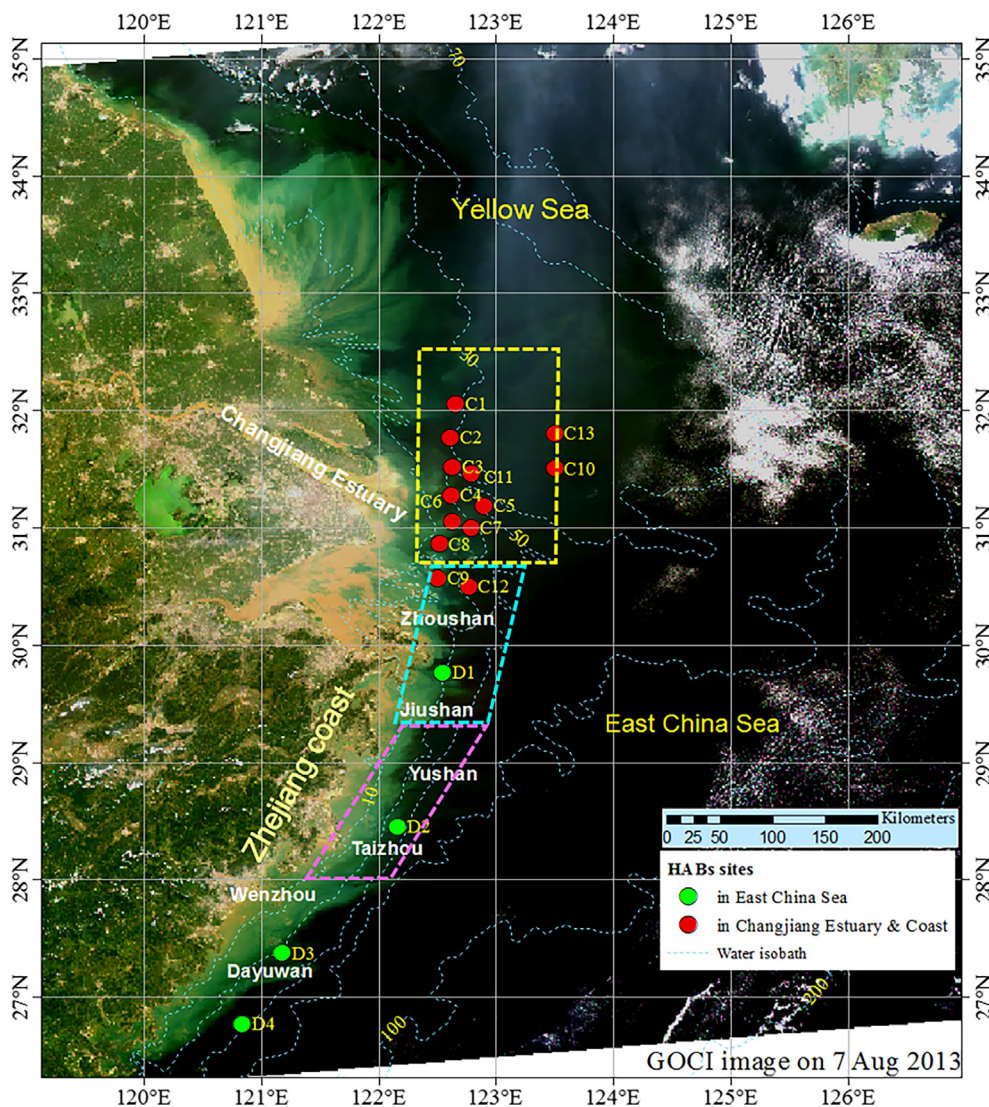


Fig. 1. Quasi-true color georeferenced GOCI image of the East China Sea (ECS) with dashed lines indicating isobaths. The solid circles depict the stations where algae blooms were observed *in situ* during two cruise campaigns carried out in the Changjiang (Yangtze) Estuary and its adjacent coast (YEC) in August 2013 (red dots, C1–13), and in the ECS in June 2014 (green dots, D1–4). Three high risk regions for algal bloom outbreaks in the ECS have been highlighted - yellow dashed line box (located in the YEC, referred to as Region A), cyan dashed line box (located in the Zhoushan coast, referred to as Region B), and violet dashed line box (located along the Zhejiang coast, referred to as Region C). (For interpretation of the references to color in this figure legend, the reader is referred to the Web version of this article.)

Table 1

Phytoplankton species observed *in situ* in August 2013 and June 2014 during cruise campaigns conducted in the YEC and the ECS. Locations of algal blooms are shown in Fig. 1.

| Algal bloom station | Dominant algal species | Class | Chla concentration ($\mu\text{g/L}$) | SPM concentration (mg/L) |
|---------------------|--|----------------|--|--------------------------|
| C1 | <i>Skeletonema costatum</i> , <i>Thalassiosira angulata</i> | Diatom | 37.73 | 11.67 |
| C2 | <i>Skeletonema costatum</i> , <i>Thalassiosira angulata</i> | Diatom | 37.42 | 13.33 |
| C3 | – | – | 14.59 | 13.50 |
| C4 | <i>Coscinodiscus jonesianus</i> , <i>Coscinodiscus oculus-iridis</i> | Diatom | 10.52 | 9.00 |
| C5 | <i>Pseudo-nitzschia pungens</i> , <i>Chaetoceros diadema</i> , <i>Thalassiosira angulata</i> | Diatom | 24.76 | 10.60 |
| C6 | <i>Prorocentrum donghaiense</i> | Dinoflagellate | 5.94 | 2.27 |
| C7 | <i>Nitzschia closterium</i> , <i>Coscinodiscus jonesianus</i> | Diatom | 16.18 | 3.50 |
| C8 | <i>Prorocentrum donghaiense</i> | Dinoflagellate | 6.04 | 6.70 |
| C9 | <i>Prorocentrum donghaiense</i> | Dinoflagellate | 15.61 | 20.25 |
| C10 | <i>Pseudo-nitzschia pungens</i> , <i>Chaetoceros diadema</i> , <i>Thalassiosira angulata</i> | Diatom | 5.63 | 0.20 |
| C11 | – | – | 6.57 | 1.25 |
| C12 | – | – | 8.18 | 12.00 |
| C13 | – | – | 5.31 | 14.60 |
| D1 | <i>Prorocentrum donghaiense</i> | Dinoflagellate | 11.30 | 27.71 |
| D2 | <i>Noctiluca scintillans</i> | Dinoflagellate | 0.10 | 8.93 |
| D3 | <i>Prorocentrum donghaiense</i> | Dinoflagellate | – | 28.49 |
| D4 | <i>Prorocentrum donghaiense</i> | Dinoflagellate | – | 9.50 |

Note: “–” indicates no information available.

Moreover, water samples collected at the 17 algal bloom stations were filtered using 25 mm Whatman GF/F Glass Microfiber Filter. The filters were kept in aluminum foil, frozen in liquid nitrogen, and then taken back to the laboratory to measure water components and concentrations. The Chla was determined in the laboratory using an F-4500 spectrofluorometer (Hitachi Inc., Japan) based on the protocols in Neveux and Lantoine (1993). The *in situ* Chla varied from 5.31 to 37.73 µg/L, with a mean value of 14.96 µg/L and a median value of 10.52 µg/L. The SPM concentration (C_{SPM}) was determined in the laboratory using the gravimetric method (Shen et al., 2010b). The *in situ* C_{SPM} ranged from 0.2 to 20.25 mg/L, with a mean value of 9.14 mg/L and a median value of 10.6 mg/L.

2.2. Algal species cultures

Three species frequently present in the algal blooms in the ECS, including the dinoflagellates, *P. donghaiense* and *K. mikimotoi*, and the diatom, *S. costatum*, were cultured in a laboratory incubator. Although we did not record the dinoflagellate, *K. mikimotoi*, in our cruise campaigns, it has been reported in the SOA's bulletins with high frequency occurrences, according to other *in situ* investigations.

The techniques used for the culture of algal species are described in detail in Andersen (2005). Seawater collected in the ECS (near 124°E, 30°N) with the salinity of 31 psu was used for the culture solution. After the seawater was filtered through a 0.22 µm Millipore polycarbonate membrane to remove impurities, the culture medium was prepared by adding the desired nutrients based on the f/2 medium formulation. The prepared culture solution was then autoclaved at 110 °C for 30 min. The algae species were cultured in a light incubator (HGZ-400, Shanghai Chuding Analytical Instrument Co., Ltd.) at a temperature of 20 °C ± 1 °C under a light intensity of 3000 lux. The light to dark cycle ratio was 12 h : 12 h.

After the stabilization of algal growth, 200–500 ml of the culture, which was diluted using the filtered seawater, was then filtered on a 25 mm Whatman GF/F Glass Microfiber Filter under low vacuum pressure. The filters were used for measuring the absorption spectra using a Lambda-1050 dual-beam UV/Vis/NIR spectrophotometer equipped with a 150 mm integrating sphere (PerkinElmer® Inc. USA). The absorption coefficients $a_{\text{ph}}(\lambda)$ were determined using the method proposed by Röttgers and Gehnke (2012). The $a_{\text{ph}}(\lambda)$ data for the three species were used to simulate their R_{rs} values.

2.3. Marine Environment Bulletin data

In situ investigations from scientific cruise campaigns could potentially miss the occurrence of some algal bloom events due to the use of cost-saving methods, inadequate number of sampling stations, and limited coverage of the extent of algal bloom distribution. Routine service-oriented environmental monitoring that is conducted by the SOA may be able to partly augment the missing data. As a result, the Chinese Marine Environment Quality Bulletin (MQB) documents have been released each year by the SOA since 1997 to provide more evidence (SOA, 1997–2017). The MQB data are collected via annual cruise campaigns, fixed stations, and buoy surveys, monitoring the marine environment in the East China Sea. Algal bloom events are recorded during concurrent surveys using cruise boats and airplanes. The area, extent, and time periods of the events are roughly estimated. Additionally, major species of algal blooms are identified. Note that the term “red tide” is often used in the MQB documents to describe microalgae bloom in China Seas. According to the statistical data documented in the MQB from 2001 to 2010, the peak in the algal bloom outbreak mainly occurs in May in the East China Sea, in terms of bloom area and numbers (Fig. 2). In this study, we have utilized a part of the data on algal blooms in the ECS documented by the MQB from 2004 to 2012 (Table 2). The objective of using this data is to aid in the verification of satellite detection of algal bloom and for the satellite differentiation of

dominant species.

2.4. Modeled remote sensing reflectance dataset

There are two approaches for modeling $R_{\text{rs}}(\lambda)$ spectra using the radiative transfer model HydroLight (Sequoia Scientific, Inc.) in this study. In order to complement the number of *in situ* data records from ship-based measurements across diverse types of optical waters, the first approach adopts bio-optical models with input parameters in Table 3 to produce general $R_{\text{rs}}(\lambda)$ spectra, namely $R_{\text{rs,gen}}$ spectra, where absorption coefficient of phytoplankton, $a_{\text{ph}}(\lambda)$, is modeled using a polynomial formula with two empirical constants, $a_0(\lambda)$ and $a_1(\lambda)$, after being normalized at a reference wavelength, e.g., 440 nm (Lee et al., 2002). The $a_0(\lambda)$ and $a_1(\lambda)$ are fitting constants that are dependent on the *in situ* dataset gathered during our investigations in the area, and we found, after an analysis of the *in situ* data, that the $a_{\text{ph}}(440)$ has a linear relationship with the Chla (Chen, 2015). The backscattering coefficient for the phytoplankton, $b_{\text{b,ph}}(\lambda)$, obeys the power-law degradation with increasing wavelength (where the reference wavelength $\lambda_0 = 660 \text{ nm}$), but shows an increase with increasing Chla (Loisel and Morel, 1998). The backscattering coefficient of non-living suspended particulate matter ($b_{\text{b,spm}}$) also complies with the power-law degradation, but the power exponent (n) decreases with an increase in SPM concentration (C_{spm}). In this study, n has a regressive function with the $b_{\text{b,spm}}$ at $\lambda_0 = 532 \text{ nm}$ (Haltrin and Kattawar, 1991), and the $b_{\text{b,spm}}(532)$ is found to change linearly with the C_{spm} , after an analysis of the *in situ* historical data in this area (Liu, 2013). The absorption coefficients of CDOM and SPM both obey the law of exponential degradation (Bricaud and Stramski, 1990; Prieur and Sathyendranath, 1981). Through analyzing regional *in situ* data, values of absorption coefficient of CDOM (a_g) at $\lambda_0 = 440 \text{ nm}$ and spectral slope (S_g) were determined in Chen and Shen (2016) and mass-specific absorption coefficient of SPM (a^*_{spm}) at $\lambda_0 = 440 \text{ nm}$ and spectral slope (S_{spm}) in (Shen et al., 2012).

Moreover, other parameters were required for HydroLight, such as sunlight incident irradiance on the sea surface $E_d(\lambda)$ that can be calculated using the RADTRAN model, sea surface wind speed (assumed as 5 m/s to calculate surface roughness), refractive index of water (given as 1.34 to calculate the Fresnel reflectance), water-air interface transmittance, and solar zenith angle (set as 30°). At the same time, it was assumed that the water was of infinite depth and was not affected by the bottom of the sea. The values for the Chla were set between 0.01 and 50 µg/L with 80 equal intervals, the values for SPM were set between 0.01 and 50 mg/L with 80 equal intervals, and the CDOM value was considered to be a constant. Therefore, a total of 6400 spectral reflectance $R_{\text{rs}}(\lambda)$ values were generated.

The second approach for modeling $R_{\text{rs}}(\lambda)$ spectra uses bio-optical properties from measurements of species cultures in the laboratory to produce specific $R_{\text{rs}}(\lambda)$ spectra, namely $R_{\text{rs,spe}}$ spectra, in order to explore spectral differences between algal species. The spectral absorption coefficients of the three species, such as the diatom, *S. costatum*, and the dinoflagellates, *P. donghaiense* and *K. mikimotoi*, came from direct measurements of mono-species cultures in the laboratory using the Lambda-1050 spectrophotometer. Regarding the spectral backscattering coefficients of the three species, we adopted separate parameterized models for diatoms and dinoflagellates based on Shang et al. (2014). In the simulation, it is assumed that there are absorption and backscattering contributions from phytoplankton, without other components like CDOM and SPM. The remaining inputs are the same as presented in Table 3. Thus, the three spectral curves of $R_{\text{rs}}(\lambda)$ are derived individually for all three species, without gradients of chlorophyll *a* and SPM concentrations, and are only used for analyzing the differences in spectral morphology.

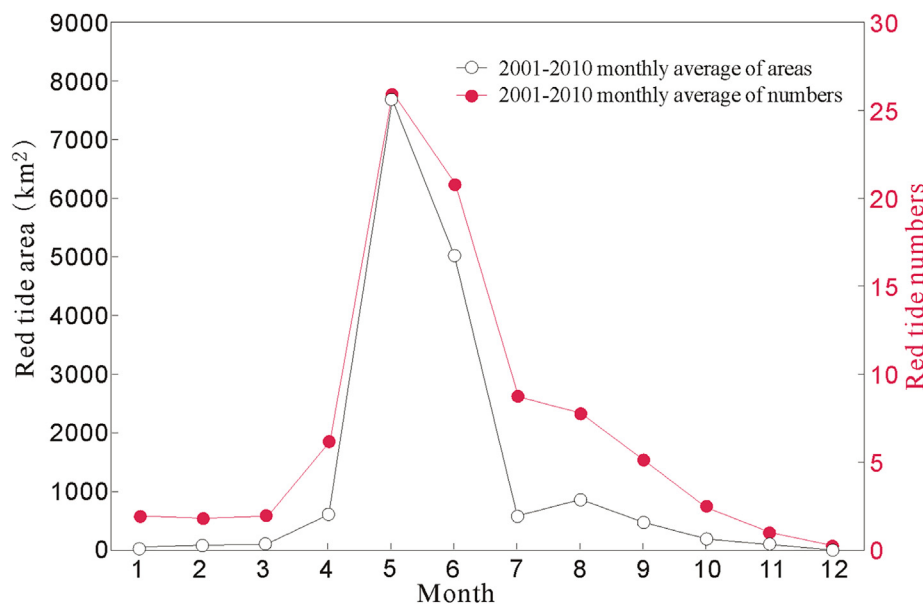


Fig. 2. Monthly averages of red tide area and numbers from 2001 to 2010, as reported in the Chinese Marine Environment Quality Bulletins in the East China Sea (reproduced). Note that the term “red tide” is used in the MQB documents to describe micro-algae bloom in China Seas. (For interpretation of the references to color in this figure legend, the reader is referred to the Web version of this article.)

2.5. MERIS, MODIS, and GOCI data

Satellite ocean color data, such as MERIS, MODIS, and GOCI data, were selected for this study. MERIS data (2003–2012) for the ECS were obtained through a cooperative Dragon program conducted by the National Remote Sensing Center of China and the European Space Agency (ESA), at the full and reduced spatial resolutions of 300 m and 1200 m with a one to three-day revisit frequency. The 15 elaborate ocean color bands that are part of the MERIS settings have the ability to observe optically complex coastal waters and the potential to identify algal bloom species. MERIS $R_{rs}(\lambda)$ outputs were obtained using the Case-2 waters regional processor (C2R) as a plug-in module of the BEAM software platform released by the ESA (Brockmann-Consult and Contributors, 2014). The retrieval algorithms for MERIS outputs obtained using the processor are described in detail in Doerffer and Schiller (2007). Although the MERIS R_{rs} outputs might be imperfect compared to the ground truth data for our coastal waters (Cui et al., 2014; Shen et al., 2010a), arithmetic calculations of waveband ratios and differences can greatly minimize this bias. Recently, an updated processor, C2RCC in the Sentinel Application Platform (SNAP), a successor of BEAM, has superseded the C2R. Through further investigation and cross-comparisons of the multi-source data, the $R_{rs}(\lambda)$ values at 560, 665, and 753 nm derived from MERIS data using the C2R for the turbid coastal waters in the YEC and ECS were more accurate than those derived using the C2RCC. In this study, we used the MERIS C2R derived $R_{rs}(\lambda)$ values.

Table 2

Algal bloom events recorded in the Chinese Marine Environment Quality Bulletins of the SOA.

| Date | Phytoplankton species | Maximum area (km^2) | Algal bloom location |
|------------------------|---|--------------------------------|--------------------------------------|
| 05.13.2004–05.26.2004 | <i>Prorocentrum donghaiense</i> | > 1000 | Zhejiang coast |
| *07.22.2004–08.20.2004 | <i>Skeletonema costatum</i> | 50 | Changjiang Estuary |
| 05.24.2005–06.01.2005 | <i>Karenia mikimotoi</i> , <i>Prorocentrum dentatum</i> | 7000 | Changjiang Estuary |
| 05.03.2006–05.06.2006 | <i>Skeletonema costatum</i> | 1000 | Zhoushan coast |
| 05.14.2006 | <i>Prorocentrum dentatum</i> | 1000 | Changjiang Estuary |
| 05.2007. | <i>Skeletonema costatum</i> | < 700 | Changjiang Estuary and Wenzhou coast |
| 05.03.2008–05.24.2008 | <i>Prorocentrum dentatum</i> | > 1150 | Zhoushan and Yushan coasts |
| 05.02.2009–05.07.2009 | — | 1330 | Yushan and Taizhou coasts |
| 05.14.2010–05.27.2010 | <i>Prorocentrum donghaiense</i> | 1040 | Zhoushan coast |
| 05.2011 | <i>Prorocentrum donghaiense</i> | < 200 | Wenzhou and Zhoushan coasts |

Note: This table only lists algal bloom data records for May from 2004 to 2011, and July to August 2004. The symbol (*) indicates that the data point, July 22, 2004, was collected from the 2004 Shanghai Bulletin of the East China Sea Branch of the SOA. Note that although *Prorocentrum dentatum* should be *P. donghaiense* in the East China Sea as proposed by Lu et al. (2005), we maintained the original descriptions as documented in the Bulletins.

Table 3

Input parameters and bio-optical models for the R_{rs} simulation using the radiative transfer model HydroLight.

| Inputs for HydroLight | Bio-optical models | References |
|--|--|---|
| Absorption coefficient of phytoplankton pigments (a_{ph}) | $a_{ph}(\lambda) = \{(a_0(\lambda) + a_1(\lambda)\ln[a_{ph}(\lambda_0)]\} \times a_{ph}(\lambda_0)$ $\lambda_0 = 440 \text{ nm}$, a_0 and a_1 : fitting constants from <i>in situ</i> data $a_{ph}(440) = 0.035 \times \text{Chla} + 0.022$ | Lee et al. (2002); Chen (2015) |
| Backscattering coefficient of phytoplankton (b_{b-ph}) | $b_{b-ph}(\lambda) = b_{ph}(\lambda) \times (b_b/b)$ $b_{ph}(\lambda) = b_0 \times (\text{Chla})^n \left(\frac{\lambda_0}{\lambda}\right)^m$ $b_0 = 0.407$, $\lambda_0 = 660$, $m = 1$, $n = 0.795$ $b_b/b = 0.005$ | Loisel and Morel (1998) |
| Backscattering coefficient of suspended particulate matter (b_{b-spm}) | $b_{b-spm}(532) = b_{spm}(532) \times (b_b/b)$ $b_{spm}(\lambda) = b_{b-spm}(\lambda_0) \left(\frac{\lambda_0}{\lambda}\right)^n$ $\lambda_0 = 532 \text{ nm}$, $b_{spm}(532) = 0.2 \times C_{spm}$ $n = 0.4114 \times b_{b-spm}(532)^{-0.3}$, $b_b/b = 0.0183$ | Haltrin and Kattawar (1991); Liu (2013) |
| Absorption coefficient of CDOM (a_g) | $a_g(\lambda) = a_g(\lambda_0) \exp(-S_g(\lambda - \lambda_0))$ $\lambda_0 = 440 \text{ nm}$, $a_g(440) = 0.25 \text{ m}^{-1}$, $S_g = 0.015$ | Prieur and Sathyendranath (1981); Bricaud and Stramski (1990); Chen and Shen (2016) |
| Absorption coefficient of SPM (a_{spm}) | $a_{spm}(\lambda) = a_{spm}(\lambda_0) \exp(-S_{spm}(\lambda - \lambda_0))$ $a_{spm}(\lambda_0) = a_{spm}^*(\lambda_0) \times C_{spm}$ $\lambda_0 = 440 \text{ nm}$, $a_{spm}^*(440) = 0.01$, $S_{spm} = 0.012$ | Prieur and Sathyendranath (1981); Shen et al. (2012) |
| Absorption coefficient of pure water (a_w) | a_w | Pope and Fry (1997) |
| Scattering coefficient of pure water (b_w) | b_w | Morel (1974) |
| Other parameters | Solar zenith angle: 30°, Wind speed: 5 m/s, Infinite depths, Ignore Raman scattering and bioluminescence | |

$[R^{-1}(\lambda_1) - R^{-1}(\lambda_2)] \times R(\lambda_3)$, was originally proposed to help estimate Chla in turbid productive waters by Gitelson et al. (2008). The rationale behind the three-band reflectance model originates from the ratio of backscattering and the sum of absorption and backscattering. The absorption property is mainly reflected in the denominator of the ratio. Therefore, with respect to chlorophyll *a*, spectral band positions within the maximum and minimum range of the chlorophyll *a* absorption coefficient can potentially be optimal candidates. As recommended in their paper, reciprocal reflectance in the first band (e.g., 660–690 nm), i.e., $R^{-1}(\lambda_1) \propto (a_{ph} + a_{dg} + a_w + b_b)/b_b$, should be maximally sensitive to absorption by chlorophyll *a*; reciprocal reflectance in the second band (e.g., 710–730 nm) should be minimally sensitive to absorption by chlorophyll *a*. In this study, we replace the recommended second band (e.g., 710–730 nm) with a band in the range of 550–570 nm. The reason of the replacement will be discussed in section 5. The purpose of subtracting $R^{-1}(\lambda_2)$ from $R^{-1}(\lambda_1)$ is to deduct the effect of $a_{spm} + a_{cdom}$, or saying, a_{dg} and b_b , assuming they are little varied in the first and second band. The third band (λ_3) should be within the range of 740–760 nm, considering the scattering effects of particulate matter.

Mostly, the mathematical relationship of the three-band blended reflectance and Chla can be regionally specific and uncertain, due to the algal diversity and the difference in water types. To simplify practical operations, we followed the concept of the three-band model and defined an index for the detection of “red tide” algal blooms (RDI):

$$\text{RDI} = \left(\frac{1}{R_{rs}(\lambda_1)} - \frac{1}{R_{rs}(\lambda_2)} \right) \times R_{rs}(\lambda_3) \quad (1)$$

Assuming the RDI index and the Chla are positively correlated, the index indicates the detection of an algal bloom when the Chla has reached a higher magnitude. The term “detection” denotes that an algal bloom is more likely to occur, but this does not mean that it definitely occurs. This is because the Chla may not be a proxy for algal cell abundance, due to the diversity in algal species and cell size.

3.2. Detection of algal blooms

Using the modeled R_{rs} -gen dataset, we calculated RDI values for the MERIS data under the following conditions - (a) the λ_1 , λ_2 , and λ_3 of Eq. (1) were set using the MERIS bands of 665, 560, and 753 nm, (b) the λ_1 , λ_2 , and λ_3 were set using the MODIS bands of 667, 555, and 748 nm, and (c) the λ_1 , λ_2 , and λ_3 were set using the GOCI bands of 660, 555, and 745 nm. We found that the RDI values estimated for MERIS, MODIS, and GOCI data have a strong correlation with the Chla in Fig. 3.

There is no standard threshold for the Chla to aid in the detection of algal bloom occurrences. This threshold is empirical, and can be derived based on regional observations and measurements. Shang et al. (2014) proposed a Chla threshold of 5 µg/L, and He et al. (2013) proposed a threshold of 10 µg/L for algal bloom detection in the East China Sea. The *in situ* data collected in our study indicates that the Chla values corresponding to algal blooms occurred in the range of 5.31–37.73 µg/L, with a median value of 10.9 µg/L. In addition, our investigation (refer to Table 1), as well as, previous studies have shown that there is no significant difference between the Chla in dinoflagellate blooms (e.g., ~9.68 µg/L from Li et al. (2010)) and in diatom blooms (e.g., ~10.96 µg/L from Lai et al. (2013)) in the ECS. Therefore, the RDI index, which is considered to be correlated to the Chla, does not differentially detect diatom and dinoflagellate blooms.

The results of the numerical experiments indicate that, in the case of Chla = 5 µg/L, the RDI estimated using MERIS bands (RDI_meris) is 0.14, and the RDI estimated using MODIS bands (RDI_modis) is 0.148 (Figs. 3a and 3b). In the case of Chla = 10 µg/L, the RDI_meris is 0.165, and the RDI_modis is 0.175. Relatively, the RDI values estimated using GOCI bands (RDI_goci) are lower than the other results, i.e. RDI_goci is 0.132 for Chla = 5 µg/L, and the RDI_goci is 0.15 for Chla = 10 µg/L (Fig. 3c). The reason for the slight difference in the three RDI values is because the MERIS, MODIS, and GOCI band positions do not accurately overlap.

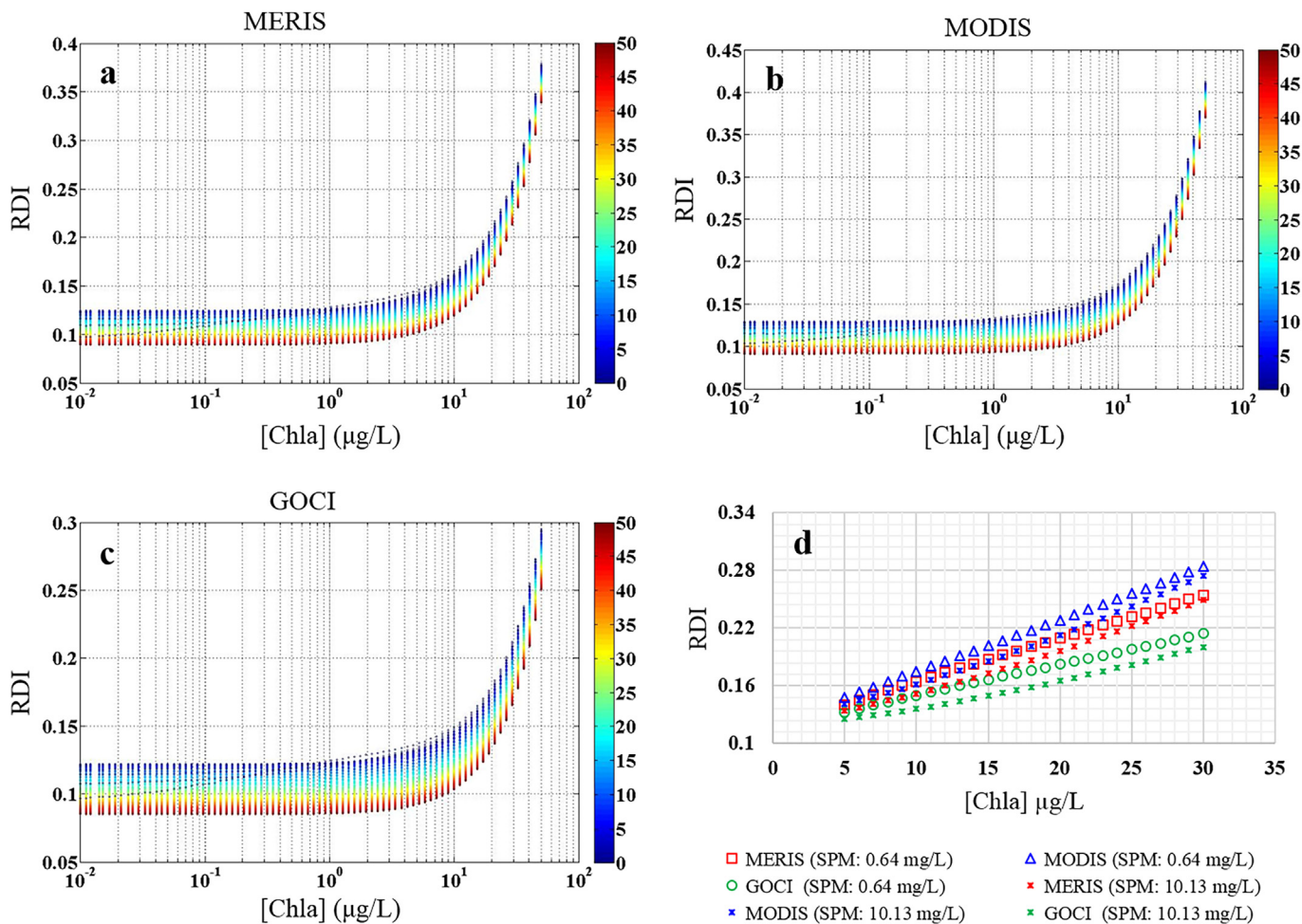


Fig. 3. Red tide detection index (RDI) and chlorophyll *a* concentration (Chla). The RDI is calculated by the three-band model using the modeled R_{rs_gen} dataset, with MERIS bands at 560, 665, and 753 nm (a), MODIS bands at 555, 667, and 748 nm (b), and GOHI bands at 555, 660, and 745 nm (c). The legend of the color scale (in a, b, and c) represents SPM concentration (mg/L). A zoomed in plot of RDI versus Chla for SPM concentrations of 0.64 mg/L and 10.13 mg/L, respectively, is shown in (d). (For interpretation of the references to color in this figure legend, the reader is referred to the Web version of this article.)

In addition, Fig. 3 shows that, for a given Chla, the RDI values will decline when the SPM values increase. Therefore, we are unable to determine a specific threshold for the Chla that can indicate an algal bloom outbreak, and we are only able to estimate RDI values from the satellite data. When the RDI_{modis} is 0.16, the corresponding Chla is 9.6 µg/L, at the mean concentration of SPM (e.g., ~10 mg/L, according to our *in situ* data), and when the RDI_{meris} is 0.16, the corresponding Chla is 11.8 µg/L at the mean SPM concentration. Therefore, it is obvious that the probability of the occurrence of algal blooms is very high when the RDI is more than 0.16.

3.3. Discrimination of phytoplankton species

In order to explore whether the three dominant species (the diatom, *S. costatum*, and the dinoflagellates, *P. donghaiense* and *K. mikimotoi*) present in algal blooms in the ECS can be discriminated, we used *in situ* R_{rs} data for *S. costatum* blooms at the C1 and C2 stations, and *in situ* R_{rs} data for *P. donghaiense* blooms at the C6, C8, C9, D1, and D4 stations (see Fig. 4a). There is no information about the algal species present at the C12 and C13 stations, but the presence of *P. donghaiense* is speculated. Unfortunately, we did not observe any *K. mikimotoi* blooms, therefore, no *in situ* R_{rs} data for *K. mikimotoi* blooms is available. Moreover, the modeled R_{rs_spe} data for all three species were used (Fig. 5b).

Although various phytoplankton species have significant differences

in R_{rs} spectral morphology (Figs. 4 and 5), this variation in spectral morphology in the range of green and red wavelengths is more appropriate for species identification, due to the strong influence of absorption in the range of 400–500 nm by CDOM and SPM components in turbid coastal waters. The wavelength for the peaks of *in situ* R_{rs} and modeled R_{rs_spe} values in the range of 550–570 nm, which occurred due to minimal absorption by phytoplankton in this spectral range (Fig. 5a), was regarded as the baseline wavelength. After normalizing R_{rs} at the baseline wavelength (e.g., 560 nm), we found that there is a pronounced difference in the normalized R_{rs} spectra in the range of 560–670 nm (Figs. 4b and 5b), which provides us with the possibility of distinguishing algal species. The normalized R_{rs} was calculated as R_{rs} at the full wavelengths divided by R_{rs} at the baseline wavelength.

The spectral slope, R_{slope} , in a range of wavelengths from λ_1 to λ_2 , was calculated as follows:

$$R_{slope} = \tan^{-1} (100 \times (1 - (R_{rs}(\lambda_2) / R_{rs}(\lambda_1))) / (\lambda_2 - \lambda_1)) \quad (2)$$

where the amplification factor (100) is set to reduce the scale differences caused by the unit of measurement of the wavelengths (nanometer). λ_1 represents the baseline wavelength in the range of 550–570 nm, and λ_2 is proposed to be a wavelength in the range of 570–670 nm.

Fig. 6 shows the spectral slope, R_{slope} , for the *in situ* R_{rs} data from the field stations, along with the R_{slope} for the modeled R_{rs_spe} of *P. donghaiense*, *S. costatum*, and *K. mikimotoi* that are labeled as Dino_P,

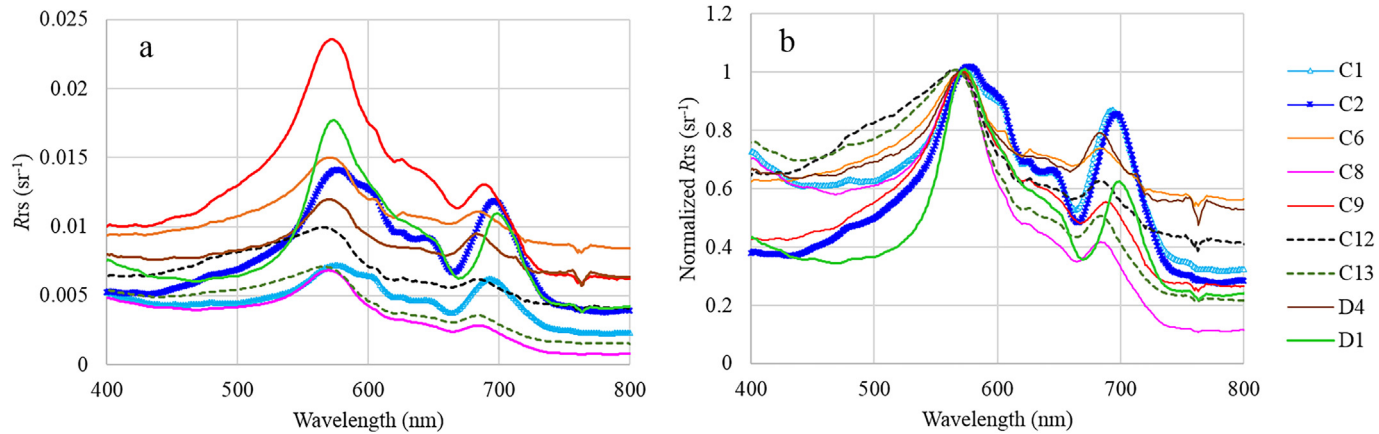


Fig. 4. R_{rs} spectra (a) and R_{rs} spectra normalized by R_{rs} at 560 nm (b) from *in situ* measurements in algal bloom waters in the YEC during the August 2013, and in the ECS during the June 2014, cruise campaigns. Locations and phytoplankton species observed at the field stations (C1, C2, etc.) are shown in Fig. 1 and Table 1.

Diat_S, and Dino_K, respectively. According to Eq. (2), the R_{slope} was calculated using the hyperspectral R_{rs} at the λ_1 of 560 nm and at the λ_2 of 605 and 610 nm, respectively. In addition, the R_{slope} was subsequently computed using MERIS bands of 560 and 620 nm, MODIS bands of 555 and 667 nm, and GOCI bands of 555 and 660 nm.

We found that the R_{slope} for *S. costatum* at the C1 and C2 field stations (< 0.4) was lower than that for *P. donghaiense* at the C6, C8, C9, C12, C13, D4, and D1 field stations (mostly > 0.4) (Fig. 6). Likewise, the R_{slope} for *S. costatum* (Diat_S) was lower than that for *P. donghaiense* (Dino_P). However, there was no obvious difference in the R_{slope} value between *S. costatum* (Diat_S) and *K. mikimotoi* (Dino_K).

Furthermore, it was found that the difference in the R_{slope} between *P. donghaiense* and *S. costatum* reduced if the second band (e.g., MODIS band at 667 nm, or GOCI band at 660 nm) was quite far away from the first band (e.g., 555 nm). Thus, the identification of *S. costatum* and *P. donghaiense* in algal blooms using MODIS and GOCI data, through the green-red spectral slope method, may not be highly accurate.

3.4. Divergence Index

We defined a Divergence Index (DI) as a logical contrary approach to the Similarity Index defined in Kirkpatrick et al. (2000), in order to analyze the impact of spectral resolution on the difference of

reflectance or absorption spectra between two phytoplankton groups or species. The DI was calculated as follows:

$$DI = \frac{1}{\pi} \times \cos\left(\frac{A \cdot B}{\|A\| \times \|B\|}\right) \quad (3)$$

where both A and B are first-order derivative vectors of the spectral curve of reflectance or absorption coefficient. A is the value for one species and B for the other.

In Eq. (3), the mathematical operations can be executed according to the following formulae, $(x \cdot y) = x_1y_1 + x_2y_2 + x_3y_3 + \dots + x_ny_n$ and $\|x\| = \sqrt{x_1^2 + x_2^2 + x_3^2 + \dots + x_n^2}$. The function of $\cos\left(\frac{A \cdot B}{\|A\| \times \|B\|}\right)$ is an angle between the A and B vectors in the range of $0 - \pi$. The DI value is in the range of 0 – 1. The higher the DI value, the more obvious the spectral signature differences are, and vice versa. Assuming that when the DI value is greater than 0.5, the probability in distinguishing algae species is higher, while the probability is very small when the value is less than 0.5.

4. Results

4.1. Detection of algal blooms using MERIS data (2003–2012)

Fig. 7 shows MERIS-derived RDI images, with minimal cloud cover,

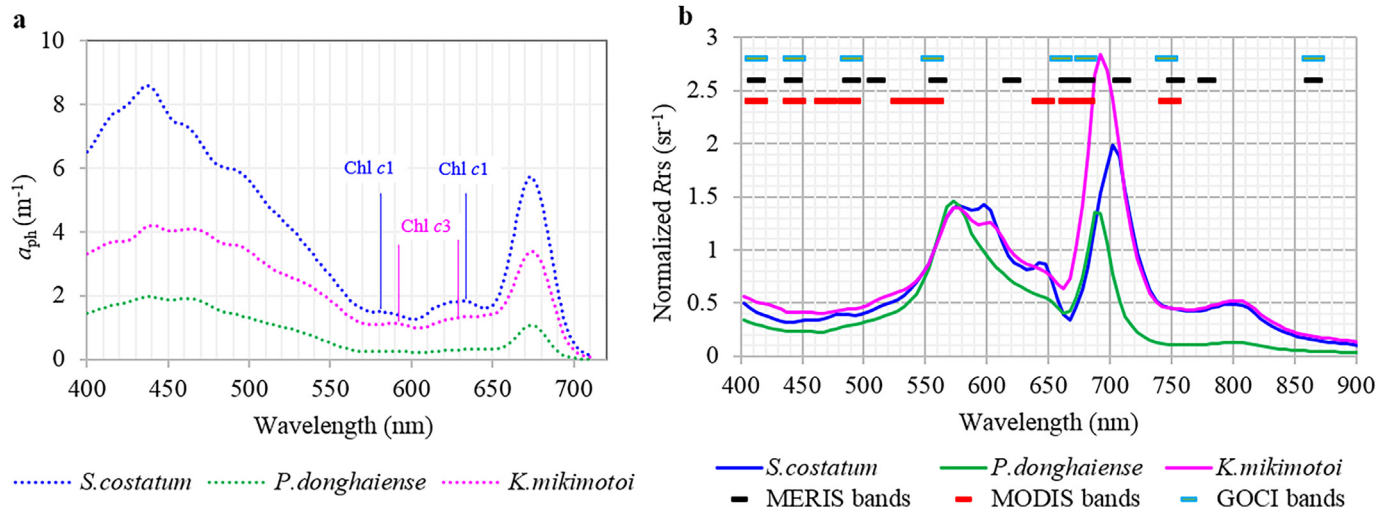


Fig. 5. (a) Laboratory measured spectra of absorption coefficient of three species, i.e., diatom, *S. costatum* (blue line), and the dinoflagellates, *P. donghaiense* (green line), and *K. mikimotoi* (pink line). In the spectral range of 550–650 nm, there are unique pigments chlorophyll c1 with peaks at 580 nm and 632 nm in *S. costatum* and chlorophyll c3 with peaks at 590 nm and 629 nm in *K. mikimotoi*. (b) Modeled R_{rs} spectra of the three species (R_{rs} -spe) normalized by the R_{rs} -spe at 560 nm. (For interpretation of the references to color in this figure legend, the reader is referred to the Web version of this article.)

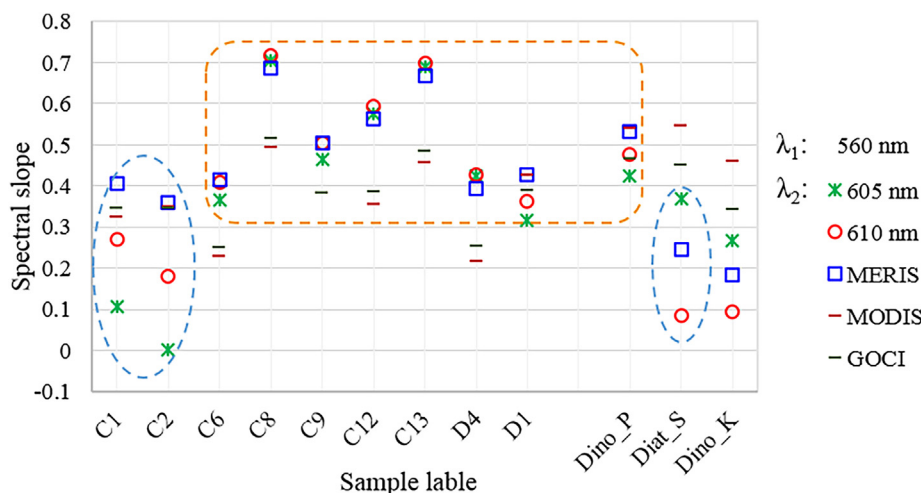


Fig. 6. Spectral slopes from the green to red range for *in situ* R_{rs} spectra of *P. donghaiense* and *S. costatum* blooms, and modeled R_{rs_spe} spectra of unicellular blooms, including species such as *P. donghaiense*, *S. costatum*, and *K. mikimotoi*. The slopes, one denoted by green stars and one by red circles, were calculated using the R_{rs} at the λ_1 of 560 nm and at the λ_2 of 605 nm and 610 nm, respectively. The slopes denoted by blue squares, orange lines, and dark lines were calculated using MERIS bands of 560 and 620 nm, MODIS bands of 555 and 667 nm, and GOCI bands of 555 and 660 nm, respectively. The points enclosed by blue dashed lines indicate samples of the diatom, *S. costatum*, with a slope below 0.4, and those enclosed by orange dashed lines indicate samples of the dinoflagellate, *P. donghaiense*, with a slope mostly greater than 0.4. (For interpretation of the references to color in this figure legend, the reader is referred to the Web version of this article.)

captured during May from 2003 to 2011. Regions with RDI values greater than 0.16 were observed to have a strip distribution along the Changjiang Estuary and the Zhejiang coast. As mentioned in Section 3.2, RDI_meris values greater than 0.16, which correspond to a Chla greater than 10 $\mu\text{g/L}$, represent areas with a very high probability of algal bloom occurrence. Although we do not have *in situ* field station data between 2003 and 2012 to validate the detection of algal blooms identified using the RDI, the location, duration, and extent of algal blooms during the peak period of algal bloom outbreaks (i.e., May) in the ECS have been investigated by the SOA since 2000. The areas highlighted using yellow rectangles in Fig. 7 were coincidentally observed and documented in the SOA's MQB, which helped provide the validation for algal bloom detection using the RDI. This implies that the RDI indicator for algal bloom detection using MERIS data has the capability to detect the location, area, and extent of algal bloom outbreaks.

To further analyze time periods and locations of algal bloom occurrences in the long term, we processed a total of 506 MERIS images available over our study area from 2003 to 2012, using the RDI identification method. As a result, 506 MERIS-derived RDI images were generated. In these images, three high risk regions (labeled A, B, and C) highlighted using three dashed line rectangles (see Fig. 1) are critical for the time series analysis of algal blooms using the RDI. The three high risk regions are located in the YEC (Region A), the Zhoushan coast (Region B), and the Zhejiang coast (Region C), where algal blooms frequently occur between late spring and early autumn (May to September). Statistical calculations of the RDI mean and the standard deviation of all pixels in the three high risk regions for each image were carried out. We found that the variation of RDI from 2002 to 2012 exists a seasonal cycle in phytoplankton growth (Fig. 8). The mean RDI values (depicted as black squares, RDI_square) in this figure exhibit a reciprocal high and low change in all three high risk regions. In Region A, the RDI value reaches the maximum peak between May and September, and reduces to the minimum peak before and after January, in most cases (Fig. 8a). In Regions B and C (Figs. 8b and 8c), the RDI maxima appear earlier, but end later compared to that in Region A, e.g. from April to October.

Using the RDI_square value as an average level might be a disadvantage, because the RDI value in some pixels within the high risk regions might be less than 0.16. We recalculated the RDI statistical averages for the three regions (depicted as red triangles, RDI_triangle), specifically for the pixels where the RDI value of each pixel was higher than the conservative threshold of 0.16. We found that the RDI_triangle values preferably demonstrated the temporal distribution of algal bloom occurrences (Fig. 8). Through the 10-year satellite observation time series data, we found that algal blooms show a long-term

consistent existence from 2003 to 2012 in all three high risk regions.

4.2. Detection of algal blooms using MERIS, MODIS, and GOCI data and *in situ* observations

Nearly synchronous MERIS, MODIS, and GOCI images, taken on September 15, 2011 over the study area, were processed to calculate RDI values (Figs. 9a-c), but we did not have any *in situ* data for that day. Fortunately, there was one GOCI image with minimal cloud cover taken on August 17, 2013, that was used to calculate the RDI value (Fig. 9d), which was then validated using *in situ* data collected in August 2013, at the field stations (see pinpoints on Fig. 9d).

After performing image segmentation with the same color density scale for the MERIS- and MODIS-derived RDI, respectively (Figs. 9a and 9b), it was found that the spatial distribution pattern of the algal bloom occurrences detected by the RDI and the RDI values in corresponding pixels, especially in the case of RDI values greater than 0.16, had a good match between the MERIS RDI and MODIS RDI images. This match implies that the RDI may suppress the bias caused by atmospheric correction to some extent, although different algorithms of atmospheric correction were employed to obtain remote sensing reflectance for MERIS and MODIS images. In the relatively clear waters of the ECS, there is not much information about phytoplankton from the MODIS-derived RDI images (e.g., off the shore of the YEC in the dark blue area in Fig. 9b). Relatively, the MERIS imagery is more capable of providing elaborate information on phytoplankton distribution under varying structures of marine currents. This might be due to the fact that MERIS data has more refined spectral resolutions and band positions. Compared with MERIS and MODIS RDI images (Figs. 9a and 9b), GOCI-derived RDI image showed a decrease in the value scale (Fig. 9c), which was also revealed by analyzing MERIS, MODIS, and GOCI data for algal bloom detection in Fig. 3d. The reasons might be attributed to the shift in wavelength positions between GOCI and the other two types of images, as well as, deviations and inconsistencies in sensor-measured spectral radiance at the junction of the wavebands arising from different sensors. Nevertheless, synchronous GOCI-derived RDI images (Fig. 9c) showed a similar distribution pattern of algal blooms as that observed in MERIS- and MODIS-derived RDI images. The RDI values derived from the GOCI image on August 17, 2013 (Fig. 9d) were consistent with the algal blooms observed at the field stations.

4.3. Discrimination of algal bloom species using satellite data and *in situ* observations

MERIS-derived spectral slope images using our proposed green-red spectral slope method are shown in Fig. 10. The spectral slope was

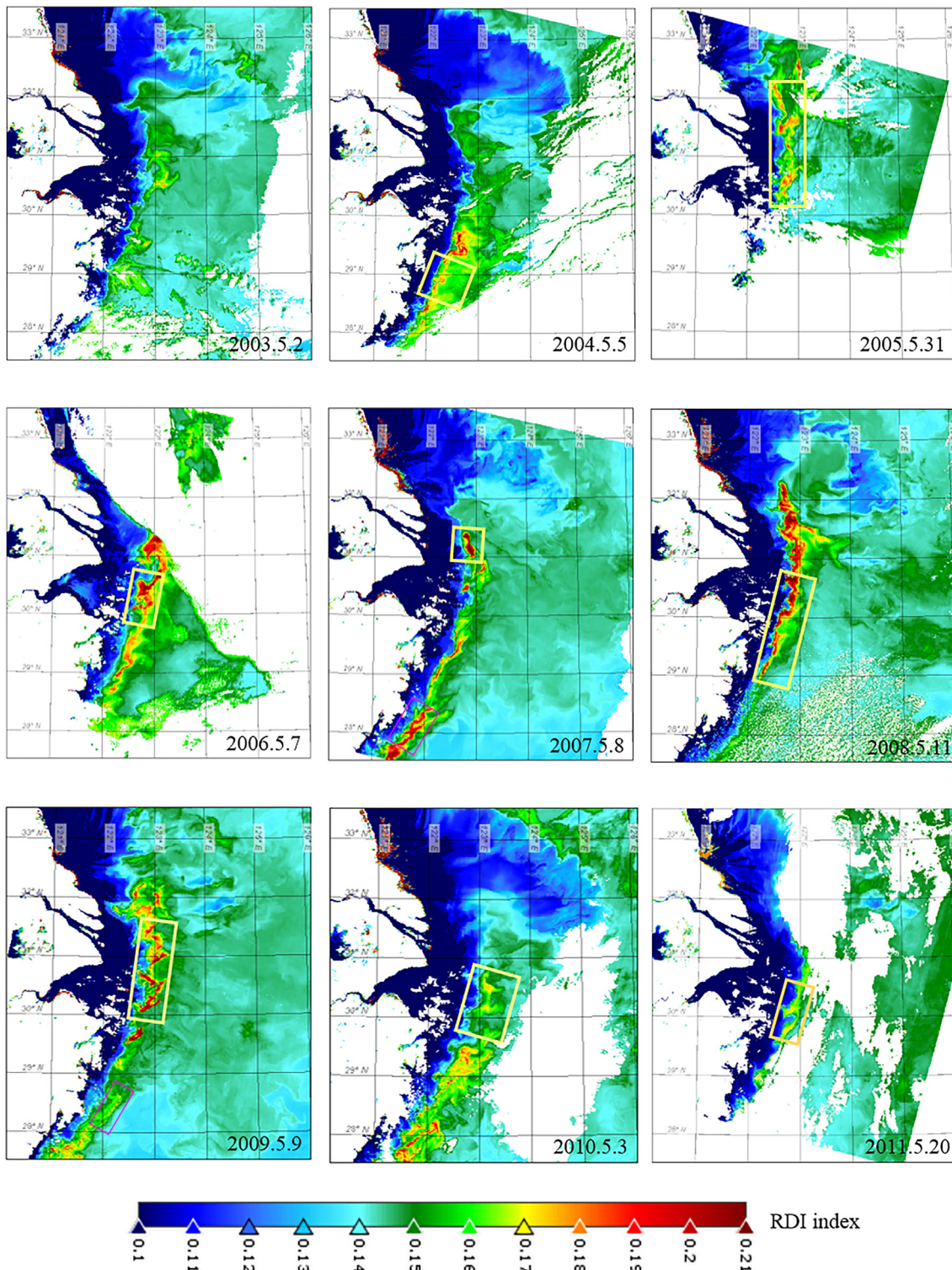


Fig. 7. Detection of algal blooms from 2003 to 2011 during the peak period of algal bloom outbreaks through MERIS-derived RDI images. The highlighted regions (yellow rectangles) in the images indicate occurrences of algal blooms that were validated and recorded during coincident surveys. These surveys are documented in the Chinese MQB data (Table 2). (For interpretation of the references to color in this figure legend, the reader is referred to the Web version of this article.)

estimated using Eq. (2). Fig. 6 shows that when the slope is lower than 0.4, the algal bloom with the diatom, *S. costatum*, as the dominant species is more likely to occur. Otherwise, the probability of occurrence of a *P. donghaiense* bloom is higher. The MERIS-identified *P. donghaiense* blooms (enclosed in yellow rectangles in Figs. 10a and 10d) were concurrently verified by SOA investigations (Table 2) carried out in May 2004, and 2008. The MERIS-identified *S. costatum* blooms

(enclosed by greenish circles in Figs. 10b and 10c) were also concurrently verified by SOA investigations (Table 2) in July 2004, and May 2007. This implies that the green-red spectral slope method for discriminating diatom and dinoflagellate species dominance in algal blooms in the ECS is effective, relatively simple, and works well, at least using MERIS data.

In addition, we derived the spectral slope for the GOCI image on

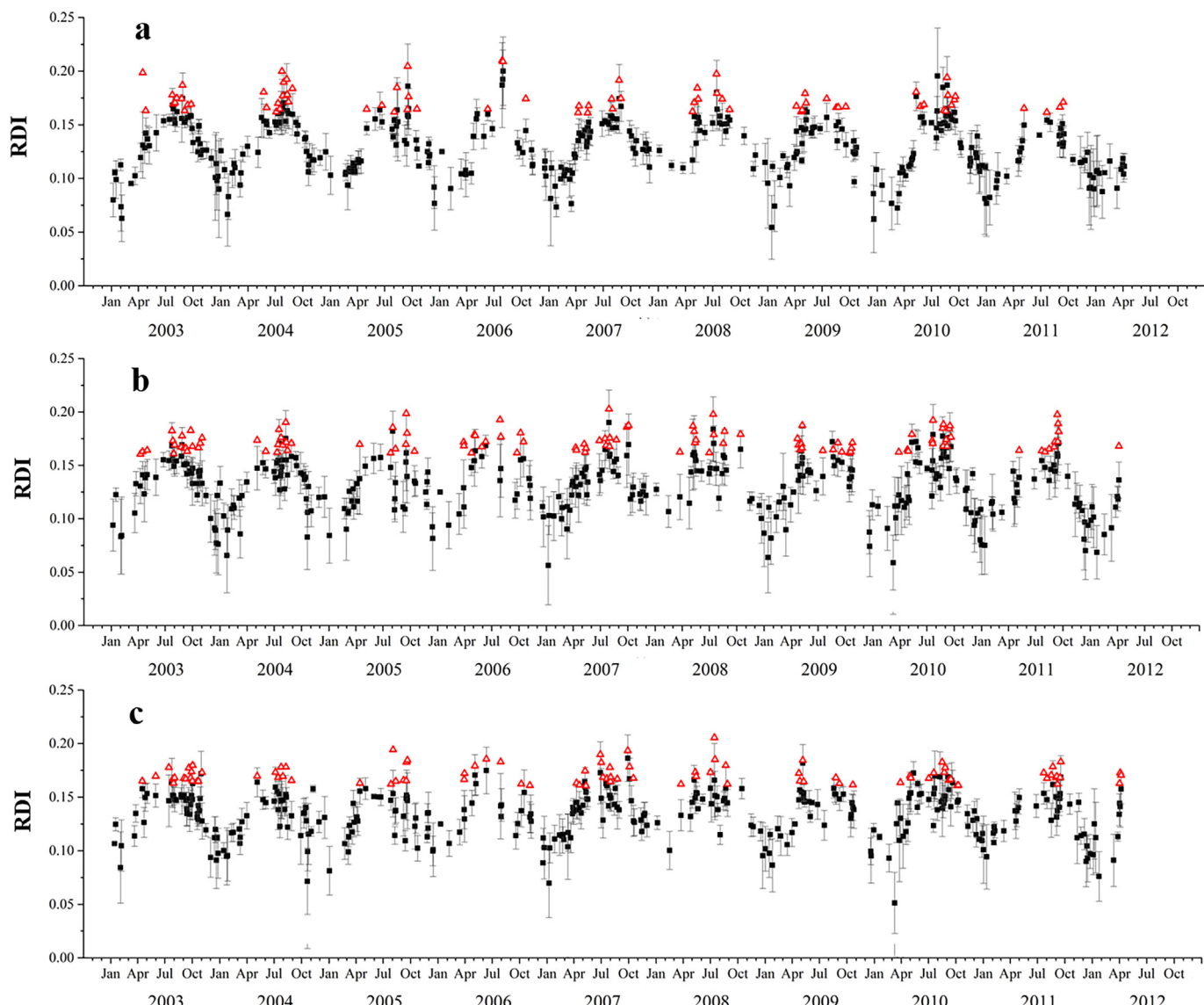


Fig. 8. MERIS-derived RDI time series outputs from 2003 to 2012 in three regions with high risk of algal bloom occurrence. The three high risk regions correspond to Region A (a), Region B (b), and Region C (c) in Fig. 1. The RDI mean values ($\text{RDI}_{\text{square}}$) and standard deviations of all pixels in the three high risk regions are illustrated by black squares and vertical biases. The RDI averages ($\text{RDI}_{\text{triangle}}$) of the pixels in the region, where the RDI value of each pixel is higher than 0.16, are denoted by red triangles. (For interpretation of the references to color in this figure legend, the reader is referred to the Web version of this article.)

August 17, 2013, since there was a simultaneous *in situ* investigation of bloom species in August 2013. The dominant algal bloom species at the C1 and C2 stations was *S. costatum*, and at the C6, C8, and C9 stations was *P. donghaiense* (pink points in Fig. 10e), which were identified during our investigation in August 2013 (in Table 1). The slope at the C1 and C2 stations was 0.48 and 0.49, respectively, and the slope at the C6, C8, and C9 stations were 0.58, 0.55, and 0.60, respectively (Fig. 10e). Although the slope values for the stations with *S. costatum* blooms were lower than those for the stations with *P. donghaiense* blooms, the GOCI discrimination for the two species was still associated with substantial uncertainties, as mentioned in Section 3.3.

4.4. Discrimination of diatom and dinoflagellate blooms using MERIS data (2003–2012)

In order to further explore the spatiotemporal distribution characteristics of algal bloom species, we calculated the spectral slope using the 10-year MERIS data for the MERIS-derived RDI over a threshold set for algal bloom detection (0.16), through the green-red spectral slope

method with MERIS bands ($\lambda_1 = 560 \text{ nm}$, $\lambda_2 = 620 \text{ nm}$). Fig. 11 illustrates the MERIS-derived slope time series data for the three high risk regions, i.e., Region A (Fig. 11a), Region B (Fig. 11b), and Region C (Fig. 11c). Fig. 11a showed that the MERIS-derived slope values cover a range of 0.1–0.9, which implies that the dominant species, *S. costatum* (represented by warm colors) and *P. donghaiense* (represented by cold colors) may frequently occur side by side in Region A. This two phase coexistence of diatom and dinoflagellate blooms generally appears in the YEC, mainly between July and August. In Figs. 11b and 11c, the MERIS-derived slope values cover a range of 0.4–0.9, which implies that the dinoflagellate, *P. donghaiense*, was less likely to dominate in the algal blooms in Region B and Region C.

5. Discussion

5.1. Identification of algal blooms

In this study, we proposed an RDI indicator based on the modified three-band model. In Eq. (1), we replace the recommended second band

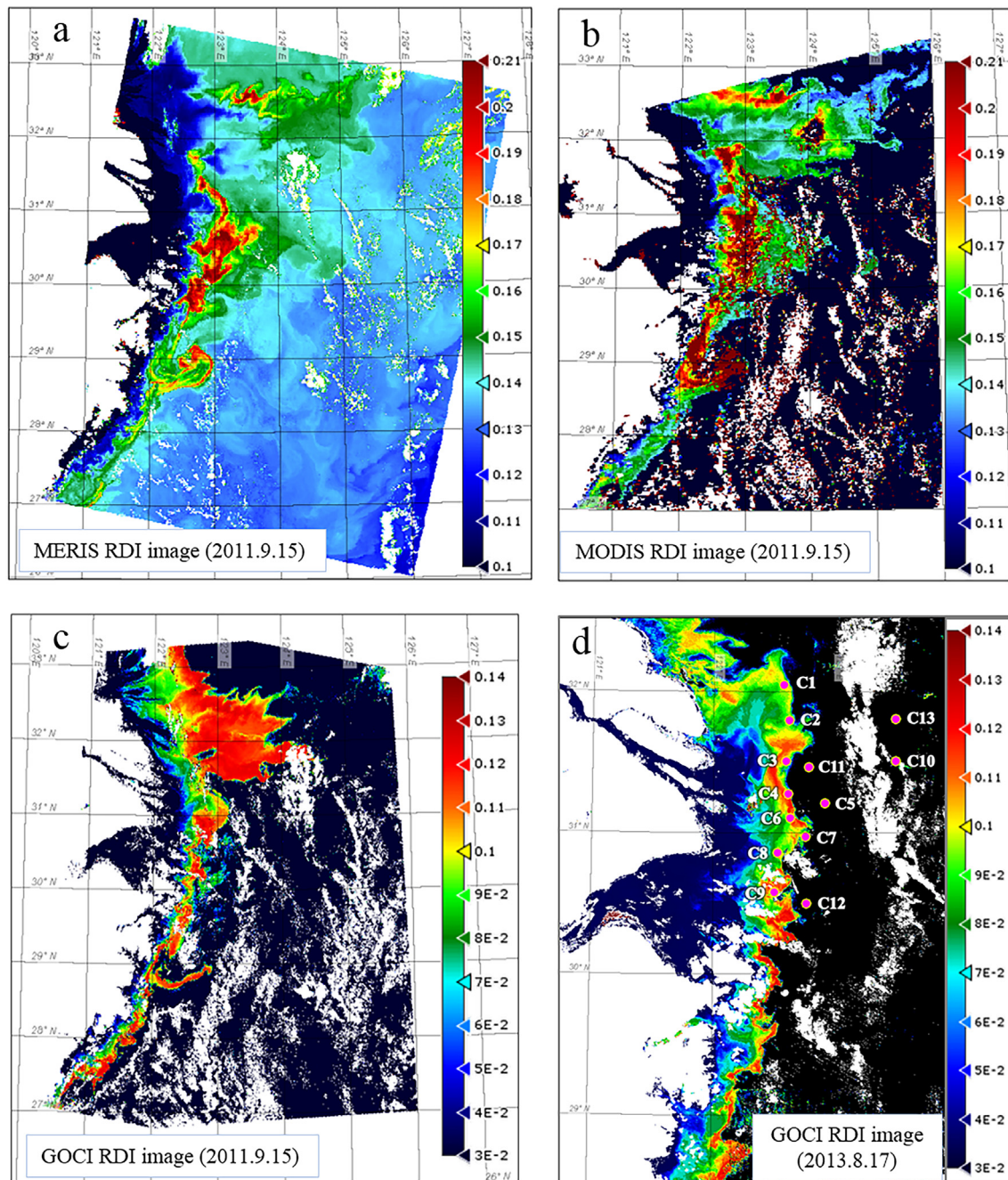


Fig. 9. Three images of algal blooms retrieved from MERIS (a), MODIS (b), and GOCI data (c) during nearly synchronous transit imagery on September 15, 2011, using the RDI index. Algal blooms observed by a GOCI-derived RDI image on August 17, 2013 (d), which was coincidentally validated by *in situ* investigations (pink pinpoints represent field stations). (For interpretation of the references to color in this figure legend, the reader is referred to the Web version of this article.)

(e.g., 710–730 nm) (Gitelson et al., 2008) with a band in the range of 550–570 nm. The reason for this substitution is that, if the second band in the range of 710–730 nm (e.g., MERIS band at 709 nm) is used, there could be a high backscattering in the range due to the presence of SPM in highly turbid waters (e.g., in the Changjiang Estuary). In this case, it may cause the higher $R_{rs}^{-1}(\lambda_2)$ value and the lower $R_{rs}^{-1}(\lambda_2)$ value. Consequently, the RDI, which is linked to the values for $R_{rs}^{-1}(\lambda_1) - R_{rs}^{-1}(\lambda_2)$, can be higher even if Chla is very low, and may enlarge with the SPM increase even if Chla is invariant. For instance, Fig. 12b shows the RDI values calculated by Eq. (1) with MERIS bands at 665 nm, 709 nm, and 753 nm for λ_1 , λ_2 , and λ_3 , respectively. Obviously, in the Changjiang Estuary with the presence of high SPM (Fig. 12a), there is a misjudgment for algal bloom detection by the RDI (within the black

circle in Fig. 12b). In this case, using MERIS band at 560 nm for λ_2 instead of the band at 709 nm, the modified three-band model can circumvent the influence of high SPM to some extent, since R_{rs} at the band of 550–570 nm is regarded as saturated (i.e., constant even if the SPM increases) when the SPM is higher than 150 mg/L (Luo et al., 2018; Shen et al., 2010b).

Moreover, the reciprocal reflection at 550–570 nm also satisfies the condition of little sensitivity to absorption by chlorophyll *a* (Fig. 5a). Assuming that absorptions by CDOM and SPM in wavelengths longer than 550 nm have less variation, the relationship between the RDI and Chla should be highly correlated. It is demonstrated in Fig. 3 that the RDIs calculated with MERIS, MODIS and GOCI bands, respectively, are indeed correlated with Chla very well. In addition, the band in the

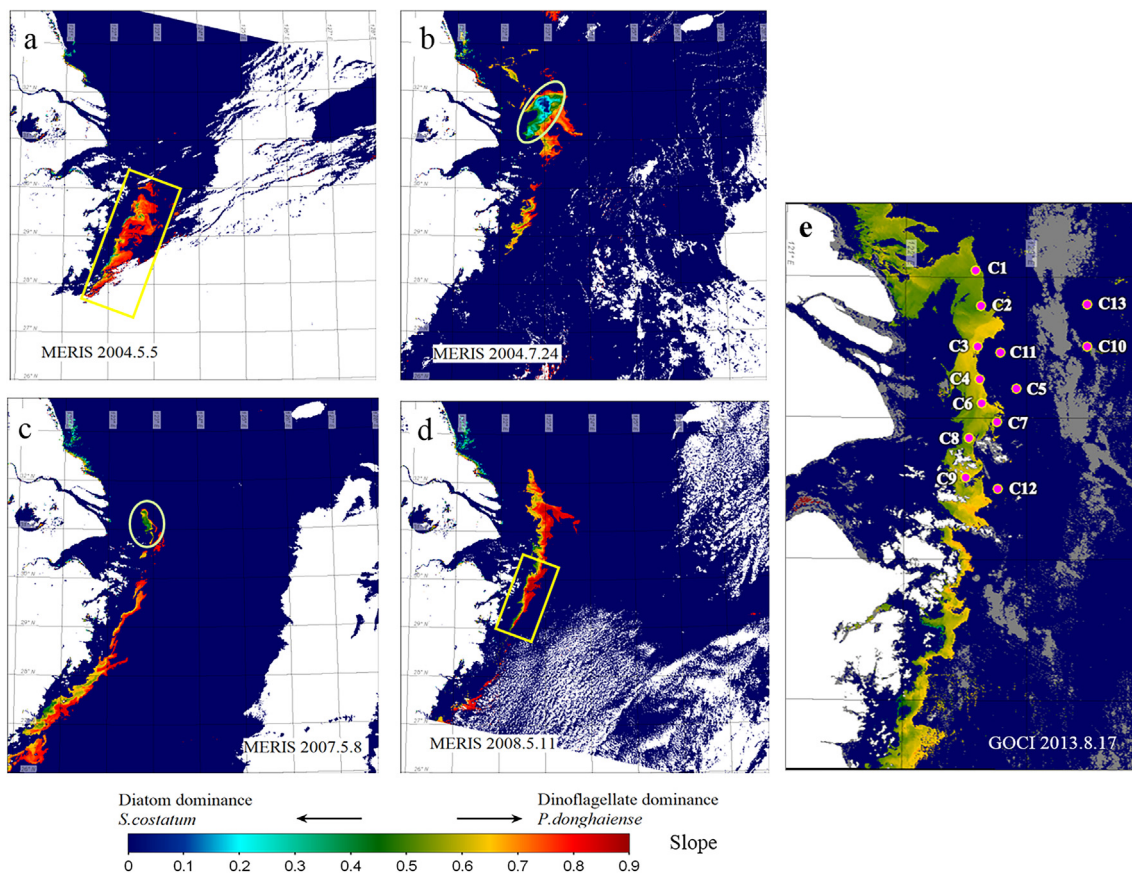


Fig. 10. Four images of MERIS-derived R_{slope} (spectral slope) on May 5, 2004 (a), July 24, 2004 (b), May 8, 2007 (c), and May 11, 2008 (d), as well as one image of GOCT-derived R_{slope} on August 17, 2013, using the green-red spectral slope method. The regions enclosed by the yellow rectangles in (a) and (d) denote *P. donghaiense* bloom areas identified by the SOA investigations (in Table 2). The regions enclosed by greenish circles in (b) and (c) denote *S. costatum* bloom areas identified by the SOA investigations (in Table 2). *S. costatum* blooms at the C1 and C2 stations, and *P. donghaiense* blooms at the C6, C8, and C9 stations (Pink points in (e)) were identified in our study in August 2013 (in Table 1). (For interpretation of the references to color in this figure legend, the reader is referred to the Web version of this article.)

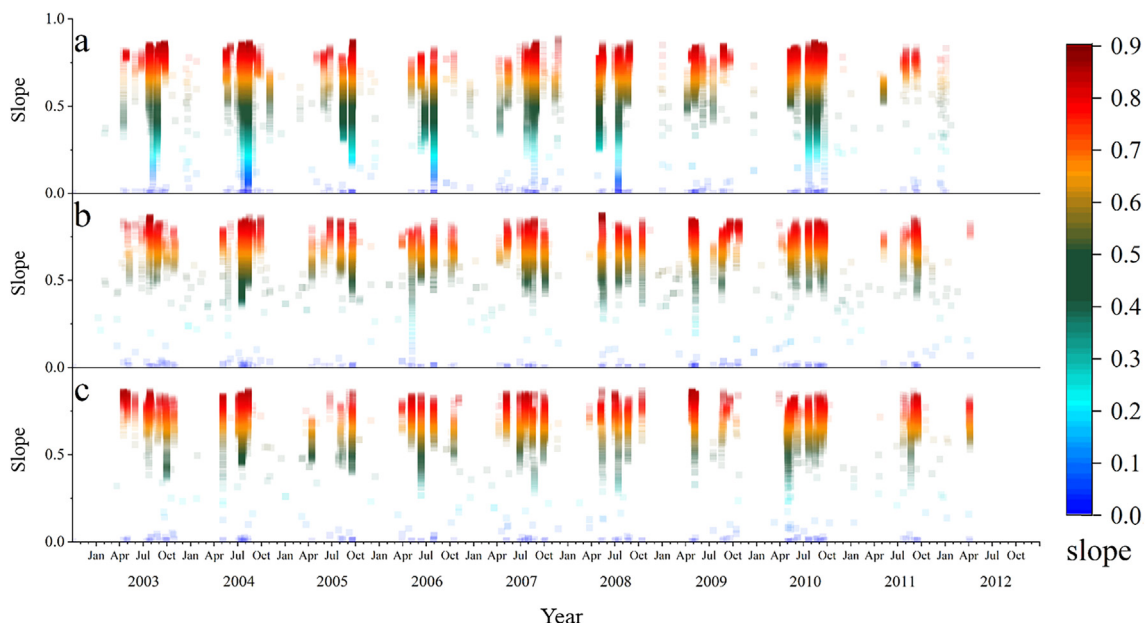


Fig. 11. 10-year MERIS-derived slope time series data from 2003 to 2012 in the three regions with high risk of algal bloom occurrence through the green-red spectral slope method. The three high risk regions correspond to Region A (a), Region B (b), and Region C (c) in Fig. 1. The y-axis and the legend for the color scale represent the spectral slope value. 30% transparency was set initially for each color in the color legend. Afterwards, the intensity of the color corresponds to the density of the spectral slope magnitude. (For interpretation of the references to color in this figure legend, the reader is referred to the Web version of this article.)

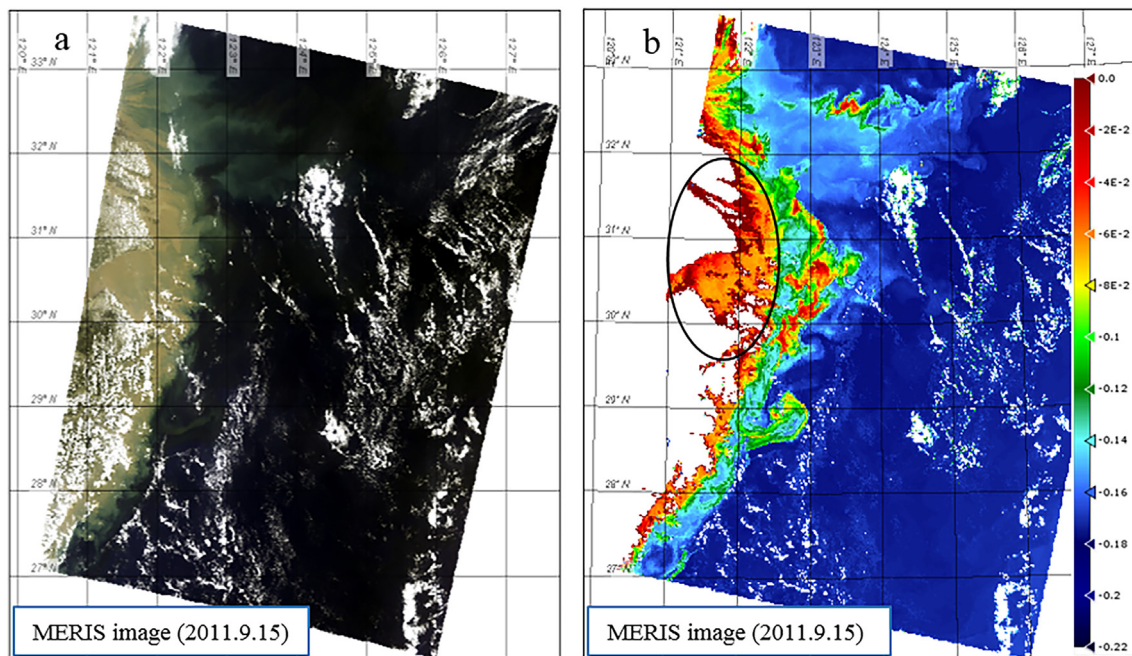


Fig. 12. (a) MERIS RGB true color image of the study area on 15 September 2011. (b) MERIS-derived RDI image with MERIS bands centered at 665 nm, 709 nm and 753 nm for λ_1 , λ_2 and λ_3 in Eq. (1). (For interpretation of the references to color in this figure legend, the reader is referred to the Web version of this article.)

range of 700–730 nm is not set up for most ocean color sensors, except the MERIS sensor.

5.2. Multi-year time series of algal blooms and bloom species

Seasonal and interannual variability of algal blooms in the eastern China seas from 1998 to 2011 was remotely sensed using 8-day composite satellite Chla (more than 10 $\mu\text{g/L}$) data for bloom analysis (He et al., 2013). The long-term time series of Chla variations and algal bloom occurrences have been poorly documented in the ECS using daily satellite data. In this study, we develop the RDI indicator instead of Chla for the bloom detection, considering problems of Chla estimates in turbid waters. Through quantitatively analyzing the 10-year time series MERIS-derived RDI changes in three high risk regions (Fig. 1), it is found in Fig. 8 that the RDI values have a pronounced cycle corresponding with climatic temperature in the coastal zones of the ECS, and values of the RDI above 0.16 mostly appear from April to September. The three high risk regions of algal blooms in the ECS we selected in this study are coincidentally in an agreement with the areas of high Bloom Occurrence Frequency (BOF) from the study of He et al. (2013) (refer to its Fig. 10) and well matched to Frequent HABs Area (FHA) from *in situ* investigations of Tang et al. (2006).

It is found in Fig. 8 that, in 2006, the earliest algal blooms in Region B and Region C anomalously occurred in March (early spring), i.e., one month earlier than normal years; while, the occurrence of earliest algal blooms in Region A was put off to June (summer), i.e., one month later than normal years. Sometimes, e.g. in 2004, the occurrences of algal blooms in Region A, Region B, and Region C synchronously started in May and ended in September. These findings for the anomalous phenomena have rarely been reported, probably because traditional investigations are poorly continuous in spatial and temporal distribution and have no advantage in a long-term time series observation of ocean color satellite with a large spatial scale.

Furthermore, the long-term time series satellite data for discrimination of diatom and dinoflagellate blooms in the ECS, which have not been reported frequently so far, exhibit a distinctive pattern of spatial and temporal distribution across the 10-year period using our proposed method. Figs. 10 and 11 indicate that diatom blooms are

mainly distributed in the north of the YEC and dinoflagellate blooms in the Zhejiang coast. The diatom and dinoflagellate blooms can co-occur in the north of the YEC. The reason behind this difference in spatial distribution mainly originates in the hydrodynamic processes that can cause a significant difference in water properties between the southern and northern coast of the Changjiang Estuary. Generally, diatoms favor niches with higher macronutrients and higher turbulence, but lower salinity and temperature compared to the dinoflagellates (Egge and Aksnes, 1992; Hinder et al., 2012; Margalef, 1978; Xie et al., 2015). During the summer (June to September), the reversal of the monsoon turns the Changjiang River plume, which has lower salinity and high nutrient content, northeastward, and the Zhejiang-Fujian Coastal current, which has higher salinity and less nutrient content, northward. The supply of silica from the Changjiang River plume is more favorable for the formation of diatom blooms in the north of the YEC. Fig. 11 shows that the dinoflagellate blooms generally start to occur in April, which is earlier than the diatom bloom, documented during *in situ* investigations by Wang et al. (2006).

In addition, the co-existence of diatom and dinoflagellate species in blooms may be a result of interspecific competition, which could lead to a transformation in bloom species dominance. It was reported that the phytoplankton community in the ECS is one of the most complex and variable communities due to the impacts of terrestrial inputs, and can appear to possess a complicated structure, in terms of the double or multiple phase mixture modes, observed in recent years during *in situ* investigations and laboratory experiments (Wang et al., 2012, 2006; Ye and Huang, 2003).

5.3. Limitations caused by spectral resolution when discriminating algal bloom species

The hyperspectral imaging data available from ocean color satellites is inadequate at the moment, therefore, extensive studies of species discrimination using remote sensing are limited. Satellite ocean color sensors with medium spectral resolutions have difficulties in discriminating phytoplankton species, especially in the presence of mixed phytoplankton species or groups.

In this study, three dominant species of algal blooms in the ECS,

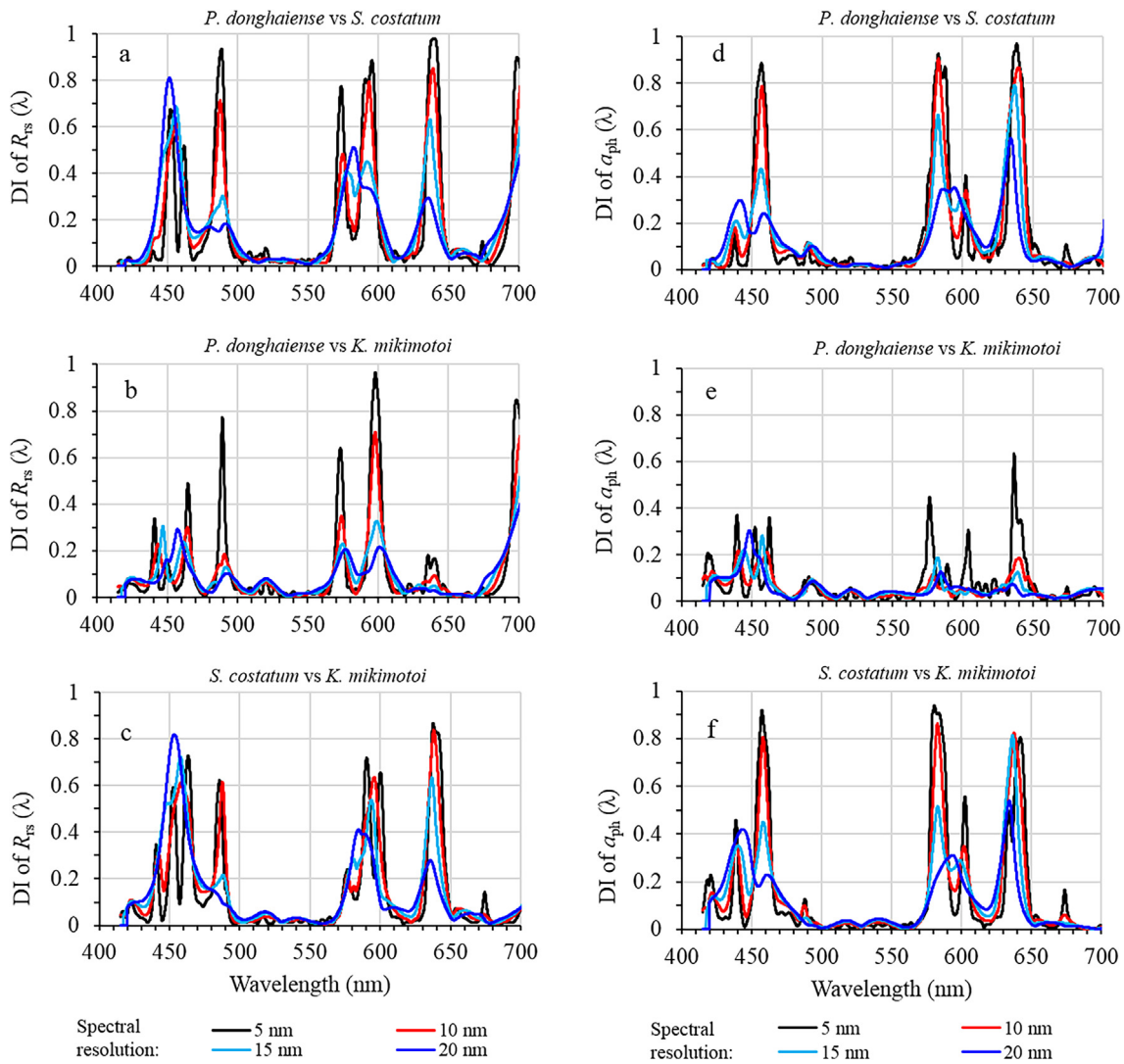


Fig. 13. Divergence index (DI) curves of remote sensing reflectance, $R_{rs}(\lambda)$ (a–c) and absorption coefficient of algae, $a_{ph}(\lambda)$ (d–e), respectively, for pairs of algal bloom species at spectral resolutions of 5, 10, 15, and 20 nm, such as dinoflagellate, *P. donghaiense* and diatom, *S. costatum* (a and d), *P. donghaiense* and *K. mikimotoi* (b and e), and *S. costatum* and *K. mikimotoi* (c and f).

including the diatom, *S. costatum*, and the dinoflagellates, *P. donghaiense*, and *K. mikimotoi*, were tested to be distinguished using the DI approach. Before performing the DI calculation according to Eq. (3), there are two steps for preprocessing hyperspectral curves. First, the hyperspectral R_{rs} (i.e., $R_{rs\text{-spe}}$) curves of the three species were filtered using a moving average algorithm (similar to a lowpass filter) in a sliding window with various spectral resolutions (e.g., 5, 10, 15, and 20 nm). Second, the first-order derivative spectra of the filtered R_{rs} were computed using the formula $\frac{dR_{rs}}{d\lambda}|_i = \frac{R_{rs}(\lambda_{i+1}) - R_{rs}(\lambda_i)}{\lambda_{i+1} - \lambda_i}$, where λ_{i+1} and λ_i are adjacent bands. Thus, the DI value of each species against the others was calculated by using the first-order derivative spectra of all three species. Furthermore, we replaced the $R_{rs\text{-spe}}$ by the absorption coefficient of each species, $a_{ph}(\lambda)$, to perform preprocessing and re-calculating of the DI value of each species against the others. The divergences between the first-order derivative spectra of $R_{rs}(\lambda)$ and $a_{ph}(\lambda)$ of *P. donghaiense* and *S. costatum*, along with the variation in wavelengths, is illustrated in detail in Figs. 13a and 13d. The divergence between *P. donghaiense* and *K. mikimotoi* is depicted in Figs. 13b and 13e, and that of *S. costatum* and *K. mikimotoi* in Figs. 13c and 13f.

Pigment composition is proven to be one of major factors that influence the spectral features in reflectance and absorption of phytoplankton (Bricaud et al., 2004), indicating that some obvious

divergences of $R_{rs}(\lambda)$ and $a_{ph}(\lambda)$ spectra in Fig. 13 are probably caused by the specific pigments of the three species.

Taken 5 nm spectral resolution as examples, a higher DI value of $a_{ph}(\lambda)$ between *P. donghaiense* and *S. costatum* in the spectral range of 440–470 nm (Fig. 13d) is due to the existence of unique pigments, such as dinoxanthin and peridinin in *P. donghaiense*, and fucoxanthin in *S. costatum* (Clementson and Wojtasiewicz, 2019; Liu, 2011; Zapata et al., 2000). Within the spectral range of 570–600 nm and 630–650 nm, the higher DI values of $a_{ph}(\lambda)$ are attributed to the existence of pigment chlorophyll c1 only in *S. costatum* (Fig. 5a). By comparison, the DI peaks of $R_{rs}(\lambda)$ correspond well with the DI peaks of $a_{ph}(\lambda)$ in the ranges of 440–470 nm, 570–600 nm, and 630–650 nm (Figs. 13a and 13d). However, the magnitude of the DI peak of $R_{rs}(\lambda)$ in the ranges of 480–495 nm largely increases. Obviously, the scattering of various algae plays a role in it and needs further study in the future.

Fig. 13e shows that the DI values of $a_{ph}(\lambda)$ between *P. donghaiense* and *K. mikimotoi* are lower in the whole visible ranges. There are slight higher DI values in the ranges of 440–470 nm, due to the existence of unique pigments dinoxanthin in *P. donghaiense*, and 19-hex-fucoxanthin, 19-but-fucoxanthin and fucoxanthin in *K. mikimotoi*, while in the narrow ranges of 570–580 nm and 630–640 nm, due to the existence of chlorophyll c3 only in *K. mikimotoi* (Fig. 5a) (Clementson and

Wojtasiewicz, 2019; Liu, 2011; Zapata et al., 2012). In comparison, although the DI peaks of $R_{rs}(\lambda)$ in the narrow ranges of 460–470 nm, 485–495 nm, 570–580 nm and 590–605 nm show prominent in the case of spectral resolution of 5 nm (Fig. 13b), it is hard to differentiate the two species if not using hyperspectral $R_{rs}(\lambda)$.

Similar to Fig. 13d, higher DI values between *S. costatum* and *K. mikimotoi* in the spectral range of 450–470 nm are attributed to unique pigments 19-but-fucoxanthin and 19-hex-fucoxanthin in *K. mikimotoi* (Fig. 13f); the higher DI value in the ranges of 580–595 nm and 630–650 nm may be caused by pigments chlorophyll c2 in *S. costatum* and chlorophyll c3 in *K. mikimotoi* (Clementson and Wojtasiewicz, 2019; Liu, 2011; Zapata et al., 2012, 2010).

Moreover, it is found that the divergences between the three species are conspicuous in the spectral range of 440–490 nm, without the influence of the CDOM and SPM components, even in the case of the spectral resolution of 20 nm in the spectral range (Figs. 13a–c). However, for optically complex coastal waters, the absence of CDOM and SPM components is almost impossible. In this case, we ought to avoid this spectral range. Fig. 13 shows that the higher DI values of $R_{rs}(\lambda)$ still exist between two of the three species in the spectral range of 560–650 nm, in which the impact of CDOM and SPM absorption on algal spectral characteristics is weak. It is obvious that the DI values of $R_{rs}(\lambda)$ for the spectral resolution of 5 nm (black lines in Figs. 13a–c) are the highest when compared to the other cases (red, cyan, and blue lines in Figs. 13a–c), and then the values gradually decrease as the spectral resolution becomes coarse. The DI of $R_{rs}(\lambda)$ for the spectral resolution of 20 nm (blue line in Figs. 13a–c) is less than 0.2 in full green and red bands, which implies that it is less likely to discriminate *P. donghaiense* from *K. mikimotoi*. Relatively, it is shown in Fig. 12a that the DI of $R_{rs}(\lambda)$ for the spectral resolution of 20 nm is about 0.5 or less in the band range of 570–610 nm, which implies that *P. donghaiense* may potentially be differentiated from *S. costatum*, but with a lower probability, similar to the discrimination of *S. costatum* from *K. mikimotoi* (the blue line in Fig. 13c). This analysis may explain that there is a high risk in distinguishing diatom and dinoflagellate blooms, e.g., *S. costatum* and *P. donghaiense* blooms, with a 20 nm spectral resolution in ocean color satellite data (e.g., GOCI data). Relatively, the DI values of $R_{rs}(\lambda)$ for the spectral resolution of 5 nm or 10 nm (red lines in Figs. 13a–c) are higher than 0.5, which implies that the possibility of discriminating one species from others is quite high, e.g., using MERIS data in this study. However, it should be noted that higher values of the DI of $R_{rs}(\lambda)$ are only observed in some narrow spectral ranges (e.g. 570–580 nm, 580–590 nm, and 635–645 nm in Fig. 13a; 595–605 nm in Fig. 13b; 585–605 nm in Fig. 13c). This shows that the positions of the bands of a satellite sensor are an important consideration when using remote sensing for the discrimination of algal species.

6. Conclusions and future outlook

Algal blooms are considered to be one of most important and critical coastal issues that need to be understood. Although the Marine Fisheries and the Environmental Protection Departments have adopted ship-based routines and helicopter-based emergency approaches for algal bloom monitoring, there are still gaps and limitations, in terms of gathering information on the spatial and temporal distribution of algal bloom outbreaks, including the location, area, duration, species, and toxins present in algal blooms. The use of satellite-based detection methods incorporated into the traditional routine monitoring procedures can clearly help fill the gaps.

In this study, we suggest the usage of the RDI indicator based on a three-band blended model, which can be applied to multi-source ocean color data, such as MERIS, MODIS, and GOCI, for algal bloom detection in turbid coastal waters. The results indicate that the RDI is effective in detecting algal blooms when using MERIS, MODIS, and GOCI data, through verification using *in situ* investigations and cross-comparisons with the multi-source data. Furthermore, we propose a method based

on a green-red spectral slope to identify the dominant species of diatom and dinoflagellate blooms in the ECS. The results demonstrate that the proposed method is simple, and feasible to aid in the differentiation of the dominant species in the diatom blooms (*S. costatum*) and the dinoflagellate blooms (*P. donghaiense*).

The MERIS 10-year time series data used for algal bloom detection from 2003 to 2012 revealed that the algal bloom occurrences had a distinct climatological cycle in the ECS. It will, therefore, be essential to investigate the response of algal blooms to climate change. Moreover, the MODIS, MERIS, and GOCI data used for algal bloom detection by applying the RDI indicator provides consistent results, which in turn encourages us to produce and merge the long-term continuous time series data of algal bloom observations from multi-sensor sources in the future, even if the limitations due to the satellites lifespan may cause a gap between the on-orbit and off-orbit satellite observations. Such long-term continuous spatiotemporal observations with extensive space coverage, in coordination with traditional monitoring procedures, should be beneficial to further understand the processes and formation mechanisms that lead to the occurrence of algal blooms.

The MERIS 10-year time series data used for the identification of the dominant diatom and dinoflagellate species in the blooms between 2003 and 2012 show that the diatom and dinoflagellate species have different spatial distributions and dissimilarities in the seasonal timing of their life cycles. These results provide the first synoptic view of the long-term time series data regarding the spatiotemporal distribution of various algal bloom species in the ECS. Although our results may be preliminary, they show that there is great potential for further studies on spatiotemporal distribution patterns and dynamics of diatom and dinoflagellate blooms in coastal oceans. These studies will be helpful in understanding the impact of climate change and anthropogenic activities on the distribution patterns in the future.

By defining and calculating the DI index, the divergence magnitudes of the reflectance spectra between two of three dominant species present in algal blooms in the ECS, including the diatom, *S. costatum*, and the dinoflagellates, *P. donghaiense*, and *K. mikimotoi*, were quantitatively assessed at various spectral resolutions (5, 10, 15, and 20 nm). Spectral resolutions higher than 10 nm should be recommended for the purpose of species discrimination. However, the setup of the band position of a satellite sensor is also crucial. Such types of analyses will help researchers understand the use of spectral resolutions, spectral ranges, and band positions for the effective discrimination of algal bloom species.

Declaration of interests

The authors declare that they have no known competing financial interests or personal relationships that could have appeared to influence the work reported in this paper.

Acknowledgments

This study is supported by National Key R&D Program of China (no. 2016YFE0103200) and National Natural Science Foundation of China (NSFC) projects (no. 41771378 and no. 51739005). The research is a part of the HYPERMAQ project (SR/00/335) of the BELSPO Research programme for earth Observation STEREO III, commissioned and financed by the Belgian Science Policy Office. We highly appreciate ESA for providing MERIS data, NASA for MODIS data and KORDI/KOSC for GOCI data. Many thanks to NSFC for providing joint cruise campaigns in the East China Sea. Our team is very grateful for data collecting and measuring in the field and laboratory. The authors greatly appreciate three anonymous reviewers and Tiit Kutser for their constructive comments and suggestions.

References

- Ahn, Y., Shanmugam, P., 2006. Detecting the red tide algal blooms from satellite ocean color observations in optically complex Northeast-Asia Coastal waters. *Remote Sens. Environ.* 103, 419–437. <https://doi.org/10.1016/j.rse.2006.04.007>.
- Andersen, R.A. (Ed.), 2005. *Algal Culturing Techniques*. Elsevier, New York.
- Blondeau-Patissier, D., Gower, J.F.R., Dekker, A.G., Phinn, S.R., Brando, V.E., 2014. A review of ocean color remote sensing methods and statistical techniques for the detection, mapping and analysis of phytoplankton blooms in coastal and open oceans. *Prog. Oceanogr.* 123, 123–144. <https://doi.org/10.1016/j.pocean.2013.12.008>.
- Bricaud, A., Claustré, H., Ras, J., Oubelkheir, K., 2004. Natural variability of phytoplanktonic absorption in oceanic waters: influence of the size structure of algal populations. *J. Geophys. Res. Oceans* 109. <https://doi.org/10.1029/2004JC002419>.
- Bricaud, A., Stramski, D., 1990. Spectral absorption coefficients of living phytoplankton and nonalgal biogenous matter: a comparison between the Peru upwelling area and the Sargasso Sea. *Limnol. Oceanogr.* 35, 562–582. <https://doi.org/10.4319/lo.1990.35.3.0562>.
- Brockmann-Consult, Contributors, 2014. BEAM ver 5.0. <http://www.brockmann-consult.de/cms/web/beam/>, Accessed date: September 2019.
- Chen, Y., 2015. Calculation of Remote Sensing Reflectance Based on Radiative Transfer Model and Analysis of Chlorophyll-A Retrieval Algorithm. Master Thesis. East China Normal University, Shanghai, China, pp. 88.
- Chen, Y., Shen, F., 2016. Influence of suspended particulate matter on chlorophyll-a retrieval algorithms in Yangtze river estuary and adjacent turbid waters. *Remote Sensing Technology and Application* 31, 126–133. <https://doi.org/10.11873/j.issn.1004-0323.2016.1.0126>.
- Clementson, L.A., Wojtasiewicz, B., 2019. Dataset on the absorption characteristics of extracted phytoplankton pigments. Data in Brief 24, 103875. <https://doi.org/10.1016/j.dib.2019.103875>.
- Cui, T., Zhang, J., Tang, J., Sathyendranath, S., Groom, S., Ma, Y., Zhao, W., Song, Q., 2014. Assessment of satellite ocean color products of MERIS, MODIS and SeaWiFS along the east China coast (in the Yellow Sea and East China sea). *Isprs J. Photogramm.* 87, 137–151. <https://doi.org/10.1016/j.isprsjprs.2013.10.013>.
- Doerffer, R., Schiller, H., 2007. The MERIS Case 2 water algorithm. *Int. J. Remote Sens.* 28, 517–535. <https://doi.org/10.1080/01431160600821127>.
- Egge, J.K., Aksnes, D.L., 1992. Silicate as regulating nutrient in phytoplankton competition. *Mar. Ecol. Prog. Ser.* 83, 281–289. <https://doi.org/10.3354/meps083281>.
- Getelson, A.A., Dall'Olmo, G., Moses, W., Rundquist, D.C., Barrow, T., Fisher, T.R., Gurlin, D., Holz, J., 2008. A simple semi-analytical model for remote estimation of chlorophyll-a in turbid waters: Validation. *Remote Sens. Environ.* 112, 3582–3593. <https://doi.org/10.1016/j.rse.2008.04.015>.
- Gower, J., King, S., Borstad, G., Brown, L., 2005. Detection of intense plankton blooms using the 709 nm band of the MERIS imaging spectrometer. *Int. J. Remote Sens.* 26, 2005–2012. <https://doi.org/10.1080/01431160500075857>.
- Hallegraeff, G.M., Anderson, D.M., Cembella, A.D. (Eds.), 2003. *Manual on Harmful Marine Microalgae*. UNESCO, Paris.
- Haltrin, V.I., Kattawar, G.W., 1991. Effects of Raman Scattering and Fluorescence on Apparent Optical Properties of Seawater. Texas A&M University.
- He, X., Bai, Y., Pan, D., Chen, C.T.A., Cheng, Q., Wang, D., Gong, F., 2013. Satellite views of the seasonal and interannual variability of phytoplankton blooms in the eastern China seas over the past 14 yr (1998–2011). *Biogeosciences* 10, 4721–4739. <https://doi.org/10.5194/bg-10-4721-2013>.
- Hinder, S.L., Hays, G.C., Edwards, M., Roberts, E.C., Walne, A.W., Gravenor, M.B., 2012. Changes in marine dinoflagellate and diatom abundance under climate change. *Nat. Clim. Chang.* 2, 271–275. <https://doi.org/10.1038/nclimate1388>.
- Hu, C., 2009. A novel ocean color index to detect floating algae in the global oceans. *Remote Sens. Environ.* 113, 2118–2129. <https://doi.org/10.1016/j.rse.2009.05.012>.
- Hu, C., Muller-Karger, F.E., Taylor, C.J., Carder, K.L., Kelble, C., Johns, E., Heil, C.A., 2005. Red tide detection and tracing using MODIS fluorescence data: a regional example in SW Florida coastal waters. *Remote Sens. Environ.* 97, 311–321. <https://doi.org/10.1016/j.rse.2005.05.013>.
- IOCCG, 2014. Phytoplankton functional types from space. In: Sathyendranath, S. (Ed.), *Reports of the International Ocean-Colour Coordinating Group*, No. 15. IOCCG, Dartmouth, Canada.
- Jackson, T., Bouman, H.A., Sathyendranath, S., Devred, E., 2011. Regional-scale changes in diatom distribution in the Humboldt upwelling system as revealed by remote sensing: implications for fisheries. *ICES J. Mar. Sci.* 68, 729–736. <https://doi.org/10.1093/icesjms/fsq181>.
- Kirkpatrick, G.J., Millie, D.F., Moline, M.A., Schofield, O., 2000. Optical discrimination of a phytoplankton species in natural mixed populations. *Limnol. Oceanogr.* 45, 467–471. <https://doi.org/10.4319/lo.2000.45.2.0467>.
- Kurekin, A.A., Miller, P.I., Van der Woerd, H.J., 2014. Satellite discrimination of Karenia mikimotoi and Phaeocystis harmful algal blooms in European coastal waters: merged classification of ocean colour data. *Harmful Algae* 31, 163–176. <https://doi.org/10.1016/j.hal.2013.11.003>.
- Lai, J., Yu, Z., Song, X., Han, X., Cao, X., Yuan, Y., 2013. Phytoplankton pigment patterns and community structure in the Yangtze estuary and its adjacent areas. *Environ. Sci.* 34, 3405–3415. <https://doi.org/10.13227/j.hjkx.2013.09.021>.
- Lee, Z., Carder, K.L., Arnone, R.A., 2002. Deriving inherent optical properties from water color: a multiband quasi-analytical algorithm for optically deep waters. *Appl. Opt.* 41, 5755. <https://doi.org/10.1364/AO.41.005755>.
- Lei, H., 2011. The Remote Sensing Algorithm of HAB Extraction Based on Inherent Optical Properties in ECS. Doctor Thesis. Zhejiang University, Hangzhou, China, pp. 131.
- Li, J., Glibert, P.M., Zhou, M., 2010. Temporal and spatial variability in nitrogen uptake kinetics during harmful dinoflagellate blooms in the East China Sea. *Harmful Algae* 9, 531–539. <https://doi.org/10.1016/j.hal.2010.03.007>.
- Liu, M., 2013. *Scattering Properties of Suspended Particles in High Turbid Waters and Remote Sensing Application*. Master Thesis. East China Normal University, Shanghai, China, pp. 80.
- Liu, S., 2011. Research and Application of Pigment Biomarkers of Common Phytoplankton Species in the Coast of China. Doctor Thesis. Ocean University of China, Qingdao, China, pp. 152.
- Liu, Y., Shen, F., Li, X., 2015. Phytoplankton light absorption properties during the blooms in adjacent waters of the Changjiang estuary. *Environ. Sci.* 36, 2019–2027.
- Loisel, H., Morel, A., 1998. Light scattering and chlorophyll concentration in case 1 waters: a reexamination. *Limnol. Oceanogr.* 43, 847–858. <https://doi.org/10.4319/lo.1998.43.5.0847>.
- Lu, D., Goebel, J., Qi, Y., Zou, J., Han, X., Gao, Y., Li, Y., 2005. Morphological and genetic study of *Prorocentrum donghaiense* Lu from the East China Sea, and comparison with some related *Prorocentrum* species. *Harmful Algae* 4, 493–505. <https://doi.org/10.1016/j.hal.2004.08.015>.
- Luo, Y., Doxaran, D., Ruddick, K., Shen, F., Gentili, B., Yan, L., Huang, H., 2018. Saturation of water reflectance in extremely turbid media based on field measurements, satellite data and bio-optical modelling. *Opt. Express* 26, 10435. <https://doi.org/10.1364/OE.26.010435>.
- Margalef, R., 1978. Life-forms of phytoplankton as survival alternatives in an unstable environment. *Oceanol. Acta* 1, 493–509.
- Morel, A., 1974. In: Jerlov, N.G., Nielsen, E.S. (Eds.), *Optical Properties of Pure Water and Pure Sea Water. Optical Aspects of Oceanography*. Academic Press, New York, pp. 1–24.
- Mouw, C.B., Greb, S., Aurin, D., DiGiocomo, P.M., Lee, Z., Twardowski, M., Binding, C., Hu, C., Ma, R., Moore, T., Moses, W., Craig, S.E., 2015. Aquatic color radiometry remote sensing of coastal and inland waters: challenges and recommendations for future satellite missions. *Remote Sens. Environ.* 160, 15–30. <https://doi.org/10.1016/j.rse.2015.02.001>.
- Neveux, J., Lantoine, F., 1993. Spectrofluorometric assay of chlorophylls and phaeopigments using the least squares approximation technique. *Deep-Sea Res. Pt. I* (40), 1747–1765. [https://doi.org/10.1016/0967-0637\(93\)90030-7](https://doi.org/10.1016/0967-0637(93)90030-7).
- Park, Y., Ahn, Y., Han, H., Yang, H., Moon, J., Ahn, J., Lee, B., Min, J., Lee, S., Kim, K., Han, T., Kim, W., Kim, J., 2014. GOCI level 2 ocean color products (GDPS 1.3) brief algorithm description (accessed June 2019). http://kosc.kiost.ac.kr/eng/p30/kosc_p34.html.
- Pope, R.M., Fry, E.S., 1997. Absorption spectrum (380–700 nm) of pure water. II. Integrating cavity measurements. *Appl. Opt.* 36, 8710–8723. <https://doi.org/10.1364/AO.36.008710>.
- Prieur, L., Sathyendranath, S., 1981. An optical classification of coastal and oceanic waters based on the specific spectral absorption curves of phytoplankton pigments, dissolved organic matter, and other particulate materials. *Limnol. Oceanogr.* 26, 671–689. <https://doi.org/10.4319/lo.1981.26.4.0671>.
- Röttgers, R., Gehnke, S., 2012. Measurement of light absorption by aquatic particles: improvement of the quantitative filter technique by use of an integrating sphere approach. *Appl. Opt.* 51, 1336. <https://doi.org/10.1364/AO.51.001336>.
- Ryan, J.P., Fischer, A.M., Kudela, R.M., Gower, J.F.R., King, S.A., Marin, R., Chavez, F.P., 2009. Influences of upwelling and downwelling winds on red tide bloom dynamics in Monterey Bay, California. *Cont. Shelf Res.* 29, 785–795. <https://doi.org/10.1016/j.csr.2008.11.006>.
- Ryu, J., Han, H., Cho, S., Park, Y., Ahn, Y., 2012. Overview of geostationary ocean color imager (GOCI) and GOCI data processing system (GDPS). *Ocean Sci. J.* 47, 223–233. <https://doi.org/10.1007/s12601-012-0024-4>.
- Sathyendranath, S., Watts, L., Devred, E., Platt, T., Caverhill, C., Maass, H., 2004. Discrimination of diatoms from other phytoplankton using ocean-colour data. *Mar. Ecol. Prog. Ser.* 272, 59–68. <https://doi.org/10.3354/meps272059>.
- SDST, MODIS Science Data Support Team <https://doi.org/10.5067/MODIS/MYD021KM.006>, <https://ladsweb.modaps.eosdis.nasa.gov/>, accessed September 2019.
- Shang, S., Wu, J., Huang, B., Lin, G., Lee, Z., Liu, J., Shang, S., 2014. A new approach to discriminate dinoflagellate from diatom blooms from space in the East China Sea. *Journal of Geophysical Research-Oceans* 119, 4653–4668. <https://doi.org/10.1002/2014JC009876>.
- Shen, F., Zhou, Y., Li, D., Zhu, W., Suhyb Salama, M., 2010a. Medium resolution imaging spectrometer (MERIS) estimation of chlorophyll-a concentration in the turbid sediment-laden waters of the Changjiang (Yangtze) Estuary. *Int. J. Remote Sens.* 31, 4635–4650. <https://doi.org/10.1080/01431161.2010.485216>.
- Shen, F., Zhou, Y., Peng, X., Chen, Y., 2014. Satellite multi-sensor mapping of suspended particulate matter in turbid estuarine and coastal ocean, China. *Int. J. Remote Sens.* 35, 4173–4192. <https://doi.org/10.1080/01431161.2014.916053>.
- Shen, F., Verhoef, W., Zhou, Y., Salama, M.S., Liu, X., 2010b. Satellite estimates of wide-range suspended sediment concentrations in Changjiang (Yangtze) estuary using MERIS data. *Estuar. Coasts* 33, 1420–1429. <https://doi.org/10.1007/s12237-010-9313-2>.
- Shen, F., Zhou, Y., Hong, G., 2012. Absorption property of non-algal particles and contribution to total light absorption in optically complex waters, a case study in Yangtze estuary and adjacent coast. *Advances in Computational Environment Science* 142, 61–66. https://doi.org/10.1007/978-3-642-27957-7_8.
- Shi, W., Wang, M., 2012. Satellite views of the Bohai Sea, Yellow Sea, and East China Sea. *Prog. Oceanogr.* 104, 30–45. <https://doi.org/10.1016/j.pocean.2012.05.001>.
- Siswanto, E., Ishizaka, J., Tripathy, S.C., Miyamura, K., 2013. Detection of harmful algal blooms of Karenia mikimotoi using MODIS measurements: a case study of Seto-Inland Sea, Japan. *Remote Sens. Environ.* 129, 185–196. <https://doi.org/10.1016/j.rse.2012.11.003>.
- SOA, 1997–2017. State oceanic administration of China. *Marine Environment Quality*

- Bulletin of China. . <http://www.nmdis.org.cn/hygb/zghyhjzlgb/>, Accessed date: September 2019.
- Sokoletsky, L.G., Shen, F., 2014. Optical closure for remote-sensing reflectance based on accurate radiative transfer approximations: the case of the Changjiang (Yangtze) River Estuary and its adjacent coastal area, China. *Int. J. Remote Sens.* 35, 4193–4224. <https://doi.org/10.1080/01431161.2014.916048>.
- Stumpf, R.P., Culver, M.E., Tester, P.A., Tomlinson, M., Kirkpatrick, G.J., Pederson, B.A., Truby, E., Ransibrahmanakul, V., Soracco, M., 2003. Monitoring Karenia brevis blooms in the Gulf of Mexico using satellite ocean color imagery and other data. *Harmful Algae* 2, 147–160. [https://doi.org/10.1016/S1568-9883\(02\)00083-5](https://doi.org/10.1016/S1568-9883(02)00083-5).
- Tang, D., Di, B., Wei, G., Ni, I., Oh, I.S., Wang, S., 2006. Spatial, seasonal and species variations of harmful algal blooms in the South Yellow Sea and East China Sea. *Hydrobiologia* 568, 245–253. <https://doi.org/10.1007/s10750-006-0108-1>.
- Tao, B., Mao, Z., Lei, H., Pan, D., Shen, Y., Bai, Y., Zhu, Q., Li, Z., 2015. A novel method for discriminating *Prorocentrum donghaiense* from diatom blooms in the East China Sea using MODIS measurements. *Remote Sens. Environ.* 158, 267–280. <https://doi.org/10.1016/j.rse.2014.11.004>.
- Tomlinson, M.C., Stumpf, R.P., Ransibrahmanakul, V., Truby, E.W., Kirkpatrick, G.J., Pederson, B.A., Vargo, G.A., Heil, C.A., 2004. Evaluation of the use of SeaWiFS imagery for detecting Karenia brevis harmful algal blooms in the eastern Gulf of Mexico. *Remote Sens. Environ.* 91, 293–303. <https://doi.org/10.1016/j.rse.2004.02.014>.
- Wang, F., Ge, W., Chai, C., Wang, J., Zhao, X., 2012. Effects of nutritional condition on the competitive parameters of *Prorocentrum donghaiense* and *Skeletonema costatum*. *Chin. J. Appl. Ecol.* 23, 1393–1399.
- Wang, M., Son, S., Shi, W., 2009. Evaluation of MODIS SWIR and NIR-SWIR atmospheric correction algorithms using SeaBASS data. *Remote Sens. Environ.* 113, 635–644. <https://doi.org/10.1016/j.rse.2008.11.005>.
- Wang, M., Shi, W., 2007. The NIR-SWIR combined atmospheric correction approach for MODIS ocean color data processing. *Opt. Express* 15, 15722. <https://doi.org/10.1364/OE.15.015722>.
- Wang, Y., Wu, H., Gao, L., Shen, F., Liang, X.S., 2019. Spatial distribution and physical controls of the spring algal blooming off the Changjiang river estuary. *Estuar. Coasts* 42, 1066–1083. <https://doi.org/10.1007/s12237-019-00545-x>.
- Wang, Z., Li, R., Zhu, M., Chen, B., Hao, Y., 2006. Study on population growth processes and interspecific competition of *Prorocentrum donghaiense* and *Skeletonema costatum* in semi-continuous dilution experiments. *Adv. Mar. Sci.* 24, 495–503.
- Xie, Y., Tilstone, G.H., Widdicombe, C., Woodward, E., Harris, C., Barnes, M.K., 2015. Effect of increases in temperature and nutrients on phytoplankton community structure and photosynthesis in the western English Channel. *Mar. Ecol. Prog. Ser.* 519, 61–73. <https://doi.org/10.3354/meps11101>.
- Ye, S., Huang, X., 2003. HABs in East China sea: surveillance and monitoring. *Mar. Environ. Sci.* 22, 10–14.
- Zapata, M., Fraga, S., Rodríguez, F., Garrido, J.L., 2012. Pigment-based chloroplast types in dinoflagellates. *Mar. Ecol. Prog. Ser.* 465, 33–52. <https://doi.org/10.3354/meps09879>.
- Zapata, M., Rodríguez, F., Garrido, J.L., 2000. Separation of chlorophylls and carotenoids from marine phytoplankton: a new HPLC method using a reversed phase C8 column and pyridine-containing mobile phases. *Mar. Ecol. Prog. Ser.* 195, 29–45. <https://doi.org/10.3354/meps195029>.